# Electron thermal transport analysis in Tokamak à Configuration Variable

E. Asp,[1,a)] J.-H. Kim,[2] W. Horton,[2] L. Porte,[1] S. Alberti,[1] A. Karpushov,[1] Y. Martin,[1] O. Sauter,[1] G. Turri,[1] and the TCV TEAM[1]

[1]*Ecole Polytechnique Fédérale de Lausanne, Centre de Recherches en Physique des Plasmas Association Euratom-Confédération Suisse, CH-1015 Lausanne, Switzerland*
[2]*Institute for Fusion Studies, University of Texas at Austin, Austin, Texas 78712, USA*

A Tokamak à Configuration Variable (TCV) [G. Tonetti, A. Heym, F. Hofmann *et al.*, in *Proceedings of the 16th Symposium on Fusion Technology, London, U.K.*, edited by R. Hemsworth (North-Holland, Amsterdam, 1991), p. 587] plasma with high power density (up to 8 MW/m$^3$) core deposited electron cyclotron resonance heating at significant plasma densities ($\leqslant 7 \times 10^{19}$ m$^{-3}$) is analyzed for the electron thermal transport. The discharge distinguishes itself as it has four distinct high confinement mode (H-mode) phases. An Ohmic H-mode with type III edge localized modes (ELMs), which turns into a type I ELMy H-mode when the ECRH is switched on. The ELMs then vanish, which gives rise to a quasistationary ELM-free H-mode. This ELM-free phase can be divided into two, one without magnetohydrodynamics (MHD) and one with. The MHD mode in the latter case causes the confinement to drop by $\sim 15\%$. For all four phases both large-scale trapped electron (TEM) and ion temperature gradient (ITG) modes and small-scale electron temperature gradient (ETG) modes are analyzed. The analytical TEM formulas have difficulty in explaining both the magnitude and the radial profile of the electron thermal flux. Collisionality governs the drive of the TEM, which for the discharge in question implies it can be driven by either the temperature or density gradient. The TEM response function is derived and it is shown to be relatively small and to have sharp resonances in its energy dependence. The ETG turbulence, predicted by the Institute for Fusion Studies electron gyrofluid code, is on the other hand driven solely by the electron temperature gradient. Both trapped and passing electrons add to the ETG instability and turbulent thermal flux. For easy comparison of the results of the above approaches and also with the Weiland model, a dimensionless error measure, the so-called average relative variance is introduced. According to this method the ETG model explains 70% of the variation in the electron heat diffusivity whereas the predictive capabilities of the TEM-ITG models are poor. These results for TCV support the conclusion that the ETG model is able to explain a wide range of anomalous electron transport data, in addition to existing evidence from ASDEX [F. Ryter, F. Leuterer, G. Pereverzev, H.-U. Fahrbach, J. Stober, W. Suttrop, and the ASDEX Upgrade Team, Phys. Rev. Lett. **86**, 2325 (2001)], Tore Supra [G. T. Hoang, W. Horton, C. Bourdelle, B. Hu, X. Garbet, and M. Ottaviani, Phys. Plasmas **10**, 405 (2003)] and the Frascati Tokamak Upgrade [A. Jacchia, F. D. Luca, S. Cirant, C. Sozzi, G. Bracco, A. Brushi, P. Buratti, S. Podda, and O. Tudisco, Nucl. Fusion **42**, 1116 (2002)]. © 2008 American Institute of Physics. [DOI: 10.1063/1.2965828]

## I. INTRODUCTION

The Tokamak à Configuration Variable (TCV) (Ref. 1) is a compact tokamak with a high power electron cyclotron resonance heating (ECRH) system that is ideally suited for basic studies of turbulent electron thermal transport. In this paper we study a new configuration of TCV which exhibits better plasma energy confinement [$H_{98(2,y)} \geqslant 1$] than previously obtained [$H_{98(2,y)} = 0.72$]. The peculiarities of this particular discharge, TCV 29892, are that it contains no less than four different high confinement mode (H-mode) phases whereof two are quasistationary without edge localized modes (ELMs).[2] The differences between this quasistationary regime and others obtained at, e.g., DIII-D (Ref. 3) and Alcator C-Mod,[4] are that on TCV it is achieved with pure electron heating, a low $q_{95}$ ($<3$), no auxiliary ion heating, no active fueling and no cryopumping. This shot is also ITER relevant as it has a hybrid scenariolike flat $q$-profile with low magnetic shear.

The TCV shot 29892 begins with a typical Ohmic H-mode with type III ELMs, but when the ECRH is turned on it switches to a type I ELMy H-mode. When the ELMs disappear a quasistationary ELM-free H-mode emerges. After a single ELM event the quasistationary ELM-free H-mode is recovered but residual magnetohydrodynamic (MHD) activity keeps the energy confinement lower than in the previous phase. The suppression of the ELMs in this case coincides with the onset of the ECRH power modulation. Nevertheless, the mechanism of the transition to a quasistationary ELM-free H-mode is not yet known as it has also been observed to arise spontaneously.[2] Although the transition to an ELM-free H-mode is an interesting topic in itself, it is out of the scope of this paper dedicated to anomalous transport.

a)Electronic mail: elina.asp@jet.efda.org.

This discharge also exhibits a higher density ($\sim 6 \cdot 10^{19}$ m$^{-3}$) than what is commonly used with ECRH heating in TCV. The use of the third harmonic (X3) heating system instead of the second harmonic system allows for strong electron heating at plasma density up to approximately $11 \cdot 10^{19}$ m$^{-3}$. This in turn also permits considerable ion heating due to thermal equilibration between ions and electrons. Unfortunately there are no charge exchange recombination spectroscopy (CXRS) measurements during this shot, that would provide profiles of carbon ion temperature, density and rotation, but they are available for a sister shot.

The core electron power deposition in this discharge varies through the four phases with an average of $1-2$ MW/m$^3$ and has a maximum of 8 MW/m$^3$ on-axis. Thus the power deposition is strongly peaked on-axis. With a core electron density, $n_e \sim 6 \cdot 10^{19}$ m$^{-3}$ this gives a heating rate of 800 keV/s per electron. The electron temperature is measured by Thomson scattering with 25 cords every 25 ms and the ECRH power deposition profile is calculated with the TORAY-GA ray-tracing code.[5]

The electron heating is well known and, together with the core deposition, gives rise to an accurately defined flow of thermal energy through the electron channel from the core plasma ($1 < T_e < 3$ keV) to the edge. This implies that there is a precise estimate of the radial electron heat flux $q_e(r)$ and also of the electron heat diffusivity $\chi_e$ as there is accurate electron temperature data (5% error). The profiles are stationary for more than five energy confinement times, $\tau_E$, and therefore the power balance $\chi_e$, neglecting the time variation, can be used. The greatest uncertainty in $q_e$ and $\chi_e$ arrives from the ambiguity of the ion temperature, $T_i$ and the intrinsic uncertainties of the measurements of the profiles' gradients. The error analysis performed shows that allowing $T_i$ to vary between $0.33 T_e$ to $T_e$ only yields a 10% error in $q_e$ in the ECRH heated phases but for the Ohmic phase the error may be considerably larger. We may nevertheless draw some conclusions as the variation in the theoretical models exceeds this uncertainty.

The TCV deuterium plasma analyzed has electron plasma beta ($\beta_e$) $> 2\%$ at the core such that $\beta_e m_i / m_e \simeq 73$, where $m_i$ and $m_e$ are the masses of ions and electrons. TCV 29892 has a toroidal magnetic field $B \simeq 1.27$ T, plasma current $I_p \simeq 400$ kA, and Alfvén velocity $v_A \ll v_e = (T_e/m_e)^{1/2}$. This implies that we have an electromagnetic regime where the Alfvén wave falls in the low parallel velocity $v_{\parallel} < v_e$ part of the electron energy distribution where electron Landau damping is significant. Hence, wave damping is important and the coupling to drift waves is strong. Due to the steep electron temperature gradient and the electron plasma pressure we expect the electromagnetic electron temperature gradient (ETG) drift-wave turbulence to be an important transport mechanism. We also enter trapped electron (TEM) and ion temperature gradient (ITG) modes in the electron energy spectrum.

The tools for the TEM-ITG analysis are an analytical model[6,7] and the fluid-based Weiland model.[8–11] For the ETG analysis we use a code based on the three coupled gyrofluid differential equations, the linear modes of which describe well the ETG instability.[12,13] This ETG code has proven itself

by accurately modelling a large database of electron thermal transport from ASDEX,[14,15] Tore Supra,[16] and the Frascati Tokamak Upgrade.[17]

To obtain a quantitative measure of how well the theoretical models explain the observed heat flux, the so-called average relative variance (ARV) (Refs. 18 and 19) is introduced. ARV gives a dimensionless error measure for inter-model comparisons. The ARV increases quadratically with the magnitude of the model $\chi_e$ so it increases with a mismatch in the model's relative error with respect to the database $\chi_e$. The magnitude of the model ETG is also in good agreement with the power balance as shown in a figure for the thermal diffusivities in Sec. III B. The ARV parameters for the analytical TEM model and the local Weiland model show that these models fail to predict quantitatively the thermal transport. The ETG model on the other hand can, according to this method, approximately explain 70% of the variation of electron heat diffusivity.

The experiment and, in particular, the confinement loss due to MHD activity is presented in Sec. II. The ETG and TEM-ITG analysis are made in Secs. III and IV, respectively. Finally conclusions are drawn in Sec. V.

## II. TCV ECRH DISCHARGES

The TCV discharge 29892 analyzed in this paper was thoroughly described by Porte *et al.* in the conference proceedings of the 21st IAEA Fusion Energy Conference.[2] This section only seeks to give the basic features of the shot needed to understand the underlying heat transport and energy confinement.

TCV is a tokamak with a powerful electron cyclotron heating (ECRH) system (see Table I), which makes it ideal to study electron heat transport properties. In shot 29892, the third-harmonic X-mode (X3) heating system was used to enable significant electron heating at density $n_e \sim 6 \cdot 10^{19}$ m$^{-3}$.[2] This results in significant ion heating through thermal equilibration, $P_{e \to i} = 0.20 \pm 0.24$ MW, if one assumes an error in $T_i$ of 20%. Ion dynamics may directly or indirectly influence the electron transport. It is also of fundamental importance for ITER and fusion producing machines in which the ion heating expected from the alpha particles through the electrons is vital to sustain the fusion reactions. In addition, this discharge features an ITER hybrid scenario $q$-profile with low magnetic shear.

X3 heating is added at $t=0.6$ s to a target plasma consisting of an Ohmic ELMy H-mode. The X3 system is operated vertically from the top of the machine with the resonating surfaces close to the plasma axis which makes the heating peak in the inner core of the plasma (Fig. 1). Moreover, the high temperature ($T_e \approx 1$ keV) caused by the high energy confinement ($\tau_E \approx 37$ ms) of the target plasma helped to increase the X3 absorption. It should be noted that the X3 heating did not produce a notable population of suprathermal electrons that may have influenced the transport analysis in the following sections.

The ion temperature profile used for the calculation of the thermal exchange power density in Fig. 1 had to be taken from a sister shot since no CXRS data was available for this

TABLE I. TCV machine and discharge 29892 parameters. Radial values are given at $r/a=0.7$.

| Fixed parameters | | |
|---|---|---|
| Plasma major radius, $R$ (m) | 0.89 | |
| Plasma minor radius, $a$ (m) | 0.22 | |
| Plasma elongation | 1.75 | |
| Plasma triangularity | 0.51 | |
| Plasma volume (m$^3$) | 1.47 | |
| Plasma current, $I_p$ (kA) | 400 | |
| Toroidal field at the magnetic axis (T) | 1.3 | |
| Time dependent parameters | $t=0.5$ s | $t=1.0$ s |
| Total heating, $P_{tot}$ (MW) | 0.49 | 1.13 |
| Global energy confinement time, $\tau_E$ (ms) | 37 | 32 |
| H-factor H$_{98(2,y)}$ | 0.72 | 1.1 |
| Safety factor, $q$ | 1.29 | 1.30 |
| Safety factor, $q_{95}$ | 2.18 | 2.16 |
| Magnetic shear, $s$ | 0.80 | 0.65 |
| Density gradient length, $L_{ne}$ (m) | 0.15 | 0.21 |
| Temperature gradient length, $L_{Te}$ m) | 0.12 | 0.09 |
| Electron temperature, $T_e$ (keV) | 0.57 | 1.3 |
| Electron diamagnetic drift velocity, $v_{de}$ (km/s) | 2.0 | 4.5 |
| Electron magnetic drift velocity, $v_{De}$ (km/s) | 0.5 | 1.3 |
| Ion Larmor radius at $T_e$, $\rho_s$ (mm) | 2.7 | 4.1 |
| Power-balance diffusivity, $\chi^{PB}$ (m$^2$/s) | 0.28 | 0.83 |
| Gyro-Bohm diffusivity, $D_{gB}=\rho_s v_{de}$ (m$^2$/s) | 5.4 | 18.5 |
| Drift wave frequency, $\omega=k_y v_{de}$ (kHz) at $k_y \rho_s=0.3$ | 341 | 353 |
| Electron collisionality, $\nu_*$ $^a$ | 0.24 | 0.06 |
| $\omega_{pe}/\omega_{ce}$ | 1.8 | 1.9 |

$^a$Refer to Eq. (18).

shot. Concerning the sister shot, the location of the plasma in the vacuum vessel only permitted the diagnostic neutral beam to measure the $T_i$ profile outside of $r/a=0.6$. Assuming that $\partial T_i/\partial r=0$ on-axis, an inward extrapolation of the profile was performed. To validate the result, the profiles were
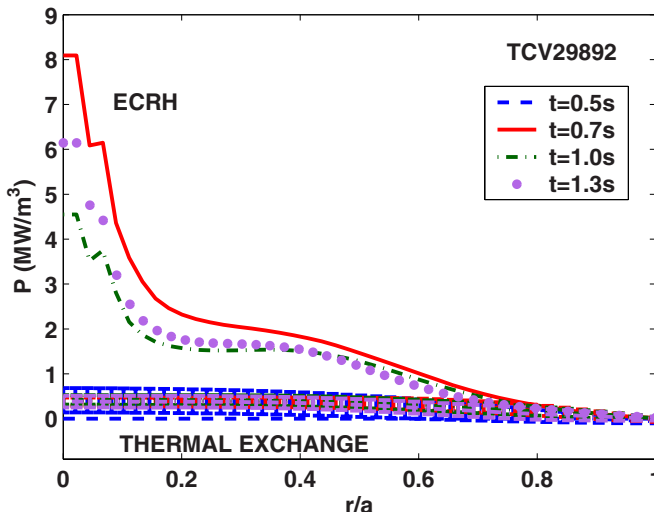


FIG. 1. (Color online) Deposition of ECRH in TCV 29892 calculated by TORAY-GA (Ref. 5) and the thermal equilibration power to the ions. The latter shows the range of values expected assuming a 5% error in $n_e$ and $T_e$ and assuming a 20% error in $T_i$.
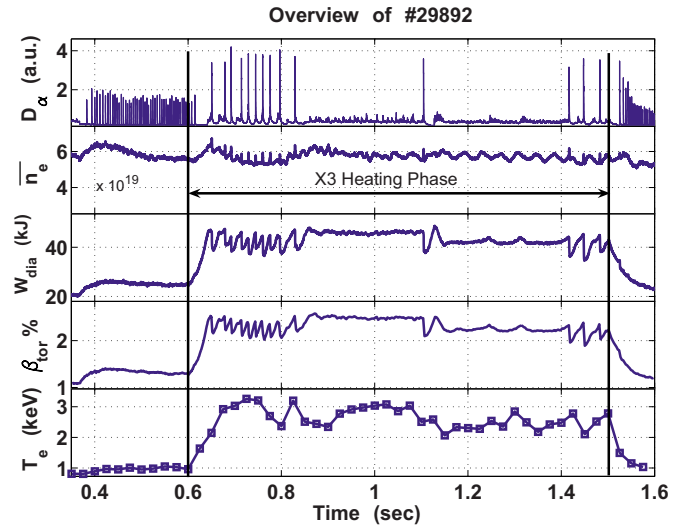


FIG. 2. (Color online) Temporal evolution of TCV29892. From top to bottom are shown $D_\alpha$ emission, line-averaged density, total stored energy measured by the diamagnetic loop, toroidal $\beta$, and on-axis electron temperature. At $t<0.6$ s, standard TCV H-mode with Type I ELMs. Full ECRH power for $0.6 \leqslant t < 0.8$ s and Type I ELMy H-mode. Modulated ECRH power for $t \geqslant 0.8$ s and quasistationary ELM-free H-mode. Single-ELM event at $t=1.1$ s triggers MHD activity which reduces the confinement as shown by the decrease in $W_{diam}$.

crosschecked with neutral particle analyser (NPA) (Ref. 20) measurements of the energy spectra of the deuterium ions escaping the plasma.

The electron heat flux is proportional to the difference between the integrated electron power deposition $P_e$ and the integrated electron-ion thermal equilibration $P_{e \to i}$, energy transfer power from electrons to ions through collisions, i.e., $q_e \sim P_e - P_{e \to i}$. During the Ohmic phase at $t=0.5$ s, the total thermal equilibration is comparable to the total power deposition $P_e=P_{oh} \sim 0.4$ MW. For the Ohmic regime, a 10% error in the ion temperature produces a 20% error in the electron heat flux. But, in the later X3-heated phases of the discharge, a 10% error in the ion temperature leads to approximately a 10% variation in the electron heat flux.

The transport analysis is carried out in each of the four H-mode phases depicted in Fig. 2. The first phase ($<0.6$ s) is a standard TCV Ohmic H-mode with type III ELMs. At $t=0.6$ s the ECRH X3 heating is switched on at full power and the plasma enters into a type I ELMy H-mode. The X3 heating is at full power ($\sim 1.35$ MW coupled to the plasma) until 0.8 s when the power from one gyrotron is fully modulated at a frequency of 127 Hz with a duty cycle of 50%. This results in an average heating power reduction of approximately 17%. Although, in this case, there was a strong correlation between X3 power modulation and the onset of the ELM-free H-mode, power modulation is not necessary.[2] The ELM-free H-mode regime has been achieved without modulation. It should be pointed out that compared to other machines like DIII-D (Ref. 3) and Alcator C-Mod,[4] which have also produced ELM-free H-modes, the TCV tokamak accomplishes this with no direct ion heating, no active fueling, and no cryopumping.
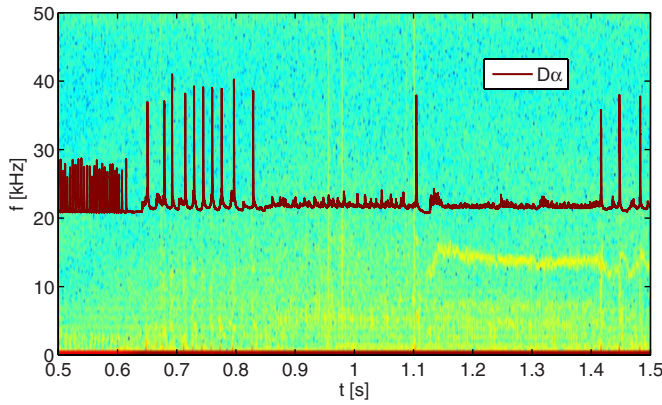
The ELM-free nature of the discharge is easily seen on

FIG. 3. (Color online) Spectral temporal evolution of TCV29892 also including the $D_\alpha$ emission [red (dark gray) line]. The $m/n=3/2$ mode with a frequency of 15 kHz emerges after the single ELM event at 1.1 s.

$$v_{E_r} = C_{E_r} T_e / eBL_{ne} \qquad (1)$$

and bound $C_{E_r}$ by 3, which is a rather generous upper limit to stay within the gyrokinetic regime. The standard tokamak core rotation is in the electron diamagnetic direction from $E_r < 0$. This upper limit to $E_r$ is then used to estimate the effect on the growth rate analytically as in Hamguchi–Horton[23] and Sugama–Horton[24] and found to lead to small effects except for weakly growing ITG modes. From the electron temperature $T_e$ profile in Fig. 4 and the system parameters in Table I, the range of the shearing frequency is $dv_{E_r}/dr = 5 \sim 8 \cdot 10^4 \text{ s}^{-1}$. This shearing rate may stabilize some of the slower growing TEM modes given in Sec. IV but in general is too low to be significantly stabilize the turbulence considered here. For ETG the effect of sheared rotation is negligible due to the fact that the electrons are interacting with much higher frequency fluctuations in a nonadiabatic electron regime.

the $D_\alpha$ signal (Fig. 2, top frame), while the high energy confinement is revealed in the measurement of total energy content obtained from a diamagnetic loop, $W_{\text{dia}}$ (third frame). The constant $W_{\text{dia}}$ and line averaged density (second frame) show that this phase is quasistationary. The phase ends with a single ELM event at 1.1 s at which time a $m/n=3/2$ MHD mode is triggered (Fig. 3). This MHD mode has a frequency of 15 kHz and a mode width of circa 5 cm.[21] An island of this width located at a normalized minor radius around $r/a = 0.6$ gives rise to a decrease of total stored energy of about 25% according to the model of Chang and Callen.[22] The observed drop in Fig. 2, third frame, is closer to 15%. There is therefore no doubt that it is the destabilization of the $m/n=3/2$ MHD mode that causes the drop in confinement in this fourth and last H-mode phase of the discharge. Note that although affected by this MHD mode, this fourth phase is a quasistationary ELM-free H-mode. Moreover, $m/n=1/1$ modes associated with sawteeth activity or intermittent $m/n=2/1$ are present throughout the discharge.[21]

For axisymmetric tokamak geometry without external toroidal momentum input the radial electric field $E_r$ is arbitrary within the ordering of $|v_{E_r}| \sim \rho_i v_i/a$. Only small deviations from axisymmetry, such as the toroidal field ripple, lead to a particular $E_r$. Thus we model

## III. ELECTRON TEMPERATURE GRADIENT TRANSPORT

In the high-$\mathbf{k}$ regime of ETG turbulence, the thermodynamics of the electron gas explains the direct drive of the turbulence from the electron temperature gradient $\nabla T_e$. It states that there is a critical temperature gradient $\nabla L_{Te}^{\text{crit}} \equiv -T_e/L_{Te}^{\text{crit}}$ for the ETG turbulence to extract energy from the temperature difference, $\Delta T = T_1 - T_2$, over the correlation length $l_c$. The Carnot cycle shown in Fig. 5 gives the upper bound on the turbulence energy $W \lesssim W_c = \Delta T \Delta S_e$, where $S_e$ is the change in the electron entropy density along the isothermal side $T_1$ in the core and $T_2$ in the lower temperature zone.[25] On the adiabatic sides of the cycle, a gas constant, $\Gamma = (d+2)/d$, describes the electron gas, where $d = 1, 2, 3$ for the number of degrees of freedom active in the ETG dynamics. Kinetic theory guides the choice of $d$ with the slab and toroidal model having $d=1$ and $d=3$, respectively. The drift-wave vortex or streamer gives the convective $\mathbf{E} \times \mathbf{B}$ motion between $(n_1, T_1)$ and $(n_2, T_2)$ producing the Carnot cycle of the convection period. From the Carnot-cycle calculation, the change of entropy density,
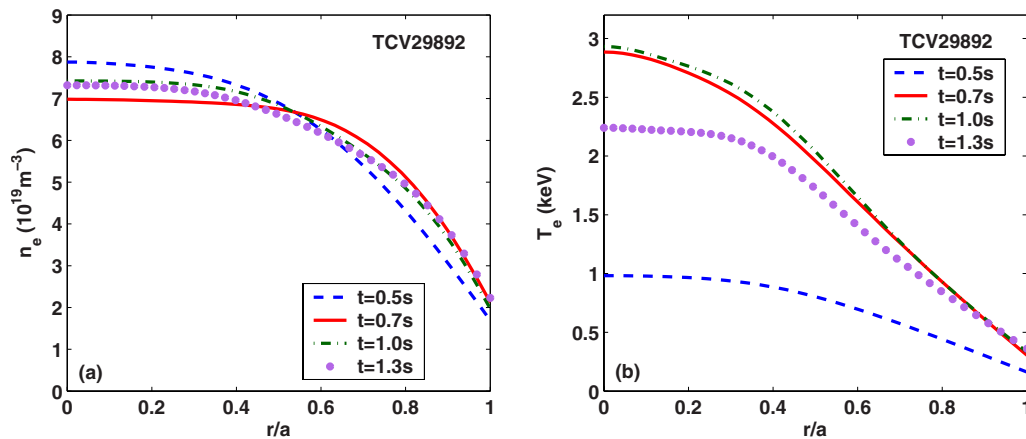


FIG. 4. (Color online) Profiles of density (left) and temperature (right) for TCV29892.
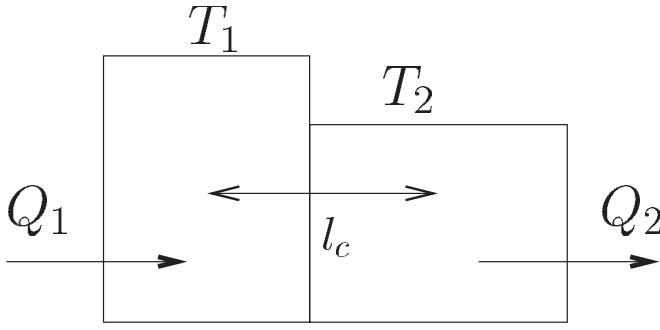
FIG. 5. Carnot cycle diagram for temperature-gradient driven drift waves. In each cycle of convection, electron heat $Q_1$ at temperature $T_1$ is taken in and convected to the lower temperature $T_2$, where $Q_2$ is exhausted.



FIG. 6. The wave frequency according to Eq. (8) for TCV29892 at $r/a=0.7$.

$$\Delta S_e = n_e k_B \left( \tfrac{3}{2} \Delta T_e / T_e - \Delta n_e / n_e \right), \tag{2}$$

for $d=3$ and $k_B$ is the Boltzmann constant. Using $T_1 - T_2 = -l_c dT_e/dr$ and $n_1 - n_2 = -l_c dn_e/dr$ give the energy density,

$$W_e = \frac{3}{2} n_e T_e l_c^2 \frac{dT_e}{dr} \left[ \frac{d \ln T_e}{dr} - \frac{2}{3} \frac{d \ln n_e}{dr} \right]. \tag{3}$$

In this ideal limit without dissipation in the system, the critical gradient expressed in terms of the major radius $R$ of the torus is

$$\frac{R}{L_{Te}^{\mathrm{crit}}} = \frac{2}{d} \frac{R}{L_{ne}}. \tag{4}$$

This critical value is expressed in terms of $\eta = L_n/L_T$ is well known from early stability analysis of both ITG and ETG. Adding dissipation induced by magnetic shear, $R/L_s = s/q$ increases the critical gradient.[25]

The role of the two space scales in the electron thermal heat flux, $q_e(r,t) = -n_e \chi_e dT_e/dr$, is made clear from the kinetic-theory formula for $q_e$. It gives the total energy flux

$$Q_e = \tfrac{3}{2} T_e \Gamma_e + q_e, \tag{5}$$

where $\Gamma_e$ is the particle flux and $q_e$ is thermal conduction. For a background of local Maxwellian electrons parameterized by $n_e$, $T_e$ and the energy density $g(\epsilon)d\epsilon$ for $\epsilon = m_e v^2 / 2T_e$, we have

$$q_e = n_e T_e \left\{ \sum_{q,\Omega} \frac{q_y |\bar\Phi_q|^2}{B T_e} f_t \int_0^\infty d\epsilon \left( \epsilon - \frac{3}{2} \right) g(\epsilon) \mathrm{Im}[h(\epsilon,q,\Omega)] \right.$$
$$\left. + \sum_{k,\omega} \frac{k_y |\Phi_k|^2}{B T_e} \int_0^\infty d\epsilon \left( \epsilon - \frac{3}{2} \right) g(\epsilon) \mathrm{Im}[h(\epsilon,k,\omega)] \right\}, \tag{6}$$

where $\int_0^\infty d\epsilon g(\epsilon) = 1$, $\bar\Phi_q$ is the bounce-averaged potential fluctuation, $f_t$ is the fraction of trapped electrons, $h(\epsilon,k,\omega)$ is the nonadiabatic electron phase-space-density response function and Im $\{\cdot\}$ is the imaginary part. We use the notation that $\omega$ and $k$ are for the small-scale high-frequency part of the fluctuation spectrum and $\Omega$, $q$ are for large-scale low-frequency part of the fluctuation spectrum.
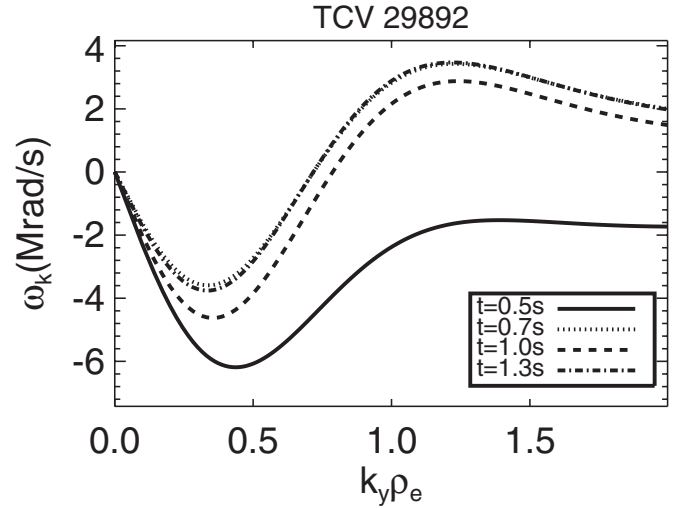
In the thermal-flux formula, the low frequency large-scale contribution arises only from the trapped electrons, since the bounce-averaged potential $\bar\Phi_q(r)=0$ for passing electrons (except for $r$ exactly on a rational surface). The small-scale response $\Phi_k$, involves resonance with both passing and trapped electrons through the response function,

$$h(\epsilon,\omega) = \frac{\left\{ \omega - \omega_{*e} \left[ 1 + \eta_e \left( \epsilon - \frac{3}{2} \right) \right] \right\} J_0^2 \left( \frac{k_\perp v_\perp}{\omega_{ce}} \right)}{\omega - \epsilon \omega_{\mathrm{De}} - k_\parallel v_\parallel + i\delta^+}, \tag{7}$$

where the wave frequency, $\omega \gg \Omega_q$ and is given approximately by

$$\omega_k = -\frac{\omega_{*e}\{ I_0(b_e)e^{-b_e} + \eta_e b_e [I_1(b_e) - I_0(b_e)]e^{-b_e} \}}{Z_{\mathrm{eff}} T_e/T_i + 1 - I_0(b_e)e^{-b_e} + k^2 \lambda_{\mathrm{De}}^2}, \tag{8}$$

where $b_e = (k_y \rho_e)^2$. Equation (8) extends up to a fraction of $v_e/L_{Te} \lesssim 10^7/\mathrm{s}$. Thus, thermal and suprathermal electrons with large and small pitch angle carry the anomalous electron heat flux in the ETG turbulence. Figure 6 yields the frequency in the case of TCV 29892 at $r/a=0.7$. For the $\eta_e$ values in this discharge, the ETG mode changes direction of rotation at $k_y \rho_e \simeq 0.3-0.8$ and this is where the linear ETG growth rate reaches a maximum. The transport flux is dominated by longer wavelength turbulence generated by the mode coupling nonlinearities as shown in the next subsection.

The effect of nonadiabatic ions occurs in the transitional region where $k_\perp \rho_i \sim 1-5$ and is associated with the part of the frequency spectrum shown in Fig. 6 where the wave propagates in the ion diamagnetic direction. In this low $k$ part of the ETG spectrum the wave resonates with guiding center drift motion of the ions with a resonant energy determined by $\omega_{k_y} = \omega_{Di}\epsilon + k_\parallel v_i \epsilon^{1/2}$, where $\epsilon = m_i v^2/(2T_i)$. Here we estimate that the guiding center drift dominates for the present conditions. In the low $k_y \rho_e$ part of the spectrum in Fig. 6 the waves are resonant with ion guiding center drifts. The resonant ions have energy $\epsilon_r = \omega_{k_y}/\omega_{Di} > 1$ in the low $k_y$ part of the spec-
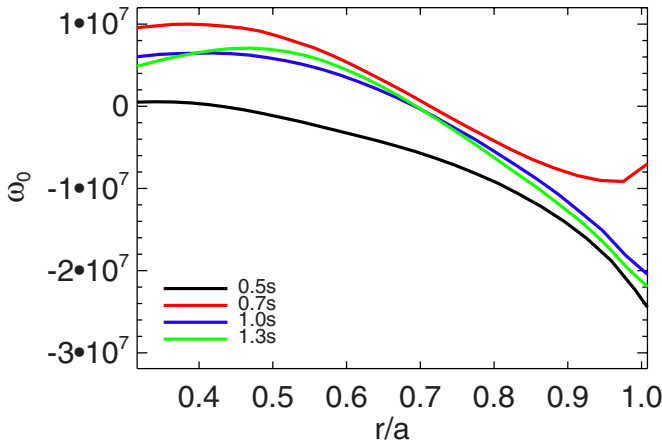
FIG. 7. (Color online) The ETG mode frequencies along the radial positions $r/a$ for $k_y\rho_e=1.0$ of TCV 29892 at $t=0.5, 0.7, 1.0,$ and 1.3 s from Eq. (8).

trum and no resonance when the direction of rotation changes to that of the electrons. These resonant ions add the dissipative response to the ion density fluctuation as given by the nonadiabatic ion response,

$$\delta n_i = -\frac{Ze\phi}{T_i}n_0\left\langle 1 - \frac{\omega_k - \omega_{*i}}{\omega_k - \omega_{Di} + i0^+}J_0^2\right\rangle. \tag{9}$$

From Eqs. (8) and (9), we can calculate, making an expansion in $\gamma_i/\omega_k$, the contribution of the resonant ions to the growth rate,

$$\gamma_i = \frac{\pi^{1/2}\omega_k(\omega_{*i} - \omega_k)}{|\omega_{Di}|(1 + b_i)^{1/2}}. \tag{10}$$

Equation (9) applies only for rotation of the mode in the ion diamagnetic direction as shown in Fig. 6 at low $k_y\rho_e$. Since the upper bound on this growth rate is $v_i R/L_{ni}L_{Ti}$ the contribution is small compared with the maximum ETG growth rate for the shorter wavelength region where the mode rotates in the electron direction. In this work we take the ions as adiabatic and plan to evaluate the full nonadiabatic response to the system in another study. This contribution to small growth rate in the stable low regions occurs in Figs. 6 and 8. At the same time this contribution gives a small particle flux due to the difference in the phase between the density fluctuation and the potential fluctuation.

## A. The electron temperature gradient model and analysis

The electron temperature gradient drift wave frequency $\omega_{0,\text{ETG}}$ given in Eq. (8) arises from the $E \times B$ convection of the electron density in the presence of adiabatic ions $\delta n_i = -eZ_i n_i\phi/T_i$. The frequency of the mode is given in Fig. 7 for $k_y\rho_e=1.0$. The smaller electron temperature gradient toward the edge gives the change of the wave direction from electron diamagnetic to ion diamagnetic drift direction.

In recent years, gyrofluid models of the ETG mode have been well developed to extend the convection fluid model for the study of drift wavelike turbulence.[26–28] Here we use a fluid model developed from the Horton's work[29–31] on ETG.

The model was used for the analysis of the Tore Supra discharges[12,25] and upgraded (Ref. 13, Chap. 3) with electron Landau damping effect[32] since then. The model is constructed in a local toroidal geometry where the magnetic curvature and grad-**B** drifts are kept but the magnetic shear is not included. Since the shear is low and positive in these discharges we have used the approximation of a constant $k_\parallel = |s|/qR$ in the analysis rather than solving the ballooning mode eigenvalue problem. This approximation is acceptable when the growth rate is not near marginal stability.[29] The higher order finite Larmor radius (FLR) dynamics is modeled by cross-field viscosities in order to absorb the energy cascaded to high $k$ wave components. The kinetic Landau damping physics is represented by the Hammett and Perkins closure model,[32] $q_\parallel = -i\sqrt{8/\pi}k_\parallel\delta T/|k_\parallel|$.

The equations of the system can be described as

$$\hat{\boldsymbol{T}}\boldsymbol{\Phi} + \hat{\boldsymbol{L}}\boldsymbol{\Phi} = \hat{\boldsymbol{N}}(\boldsymbol{\Phi},\boldsymbol{\Phi}), \tag{11}$$

where $\hat{\boldsymbol{T}}$, $\hat{\boldsymbol{L}}$, and $\hat{\boldsymbol{N}}$ are a temporal operator, a linear spatial operator, and a nonlinear spatial operator, respectively.

The radial and poloidal position $(x, y)$, the toroidal position $z$, and time $t$ are normalized by the electron gyroradius $\rho_e$, electron density gradient length $L_n$ and $L_n/v_{Te}$. The field vector $\boldsymbol{\Phi} = (\phi, A_\parallel, \delta T_e)$ consists of the electrostatic fluctuation $\phi$, the parallel magnetic potential fluctuation $A_\parallel$, and the electron temperature fluctuation $\delta T_e$, all of which are normalized by $T_e/e$, $\beta_e T_e/ev_{Te}$ and $T_e$ with the additional factor $\rho_e/L_n$,

$$\hat{\boldsymbol{T}}_{11} = (-1 + \nabla_\perp^2)\frac{\partial}{\partial t}, \quad \hat{\boldsymbol{T}}_{22} = \left(-\frac{\beta_e}{2} + \nabla_\perp^2\right)\frac{\partial}{\partial t},$$

$$\hat{\boldsymbol{T}}_{33} = \frac{\partial}{\partial t} \quad \text{and} \quad \hat{\boldsymbol{T}}_{ij} = 0 \quad \text{where} \quad i \neq j,$$

$$\hat{\boldsymbol{L}}_{11} = \left\{1 - 2\epsilon_n + (1 + \eta_e)\nabla_\perp^2\frac{\partial}{\partial y}\right\} - \mu\nabla^4,$$

$$\hat{\boldsymbol{L}}_{12} = \nabla_\perp^2\frac{\partial}{\partial z}, \quad \hat{\boldsymbol{L}}_{13} = 2\epsilon_n\frac{\partial}{\partial y}, \tag{12}$$

$$\hat{\boldsymbol{L}}_{21} = -\frac{\partial}{\partial z}, \quad \hat{\boldsymbol{L}}_{22} = -\frac{\beta_e}{2}(1 + \eta_e)\frac{\partial}{\partial y} + \frac{\eta}{\mu}\nabla_\perp^2, \quad \hat{\boldsymbol{L}}_{23} = \frac{\partial}{\partial z},$$

$$\hat{\boldsymbol{L}}_{31} = [\eta_e - 4\epsilon_n(\Gamma - 1)]\frac{\partial}{\partial y}, \quad \hat{\boldsymbol{L}}_{32} = (\Gamma - 1)\nabla_\perp^2\frac{\partial}{\partial z},$$

$$\hat{\boldsymbol{L}}_{33} = 2\epsilon_n(\Gamma - 1)\frac{\partial}{\partial y} - \chi_\perp\nabla_\perp^2 - \frac{\partial^2}{\partial z^2} - (\Gamma - 1)\sqrt{\frac{8}{\pi}}|k_\parallel|,$$

where electron plasma beta $\beta_e = 2\mu_0 p_e/B^2$, the ratio of electron and ion temperature $\tau = T_e/T_i$ and the ratio of electron density gradient length $L_n$ and magnetic field gradient $R$, $\epsilon_n = L_n/R$. Viscosity $\mu$, resistivity $\eta/\mu$, and heat diffusivity $\chi_\perp$ are included,

$$\hat{\boldsymbol{N}}_1 = \hat{\boldsymbol{N}}_{111} + \hat{\boldsymbol{N}}_{122} = -[\phi, \nabla_\perp^2\phi] + \frac{\beta_e}{2}[A_\parallel, \nabla_\perp^2 A_\parallel],$$
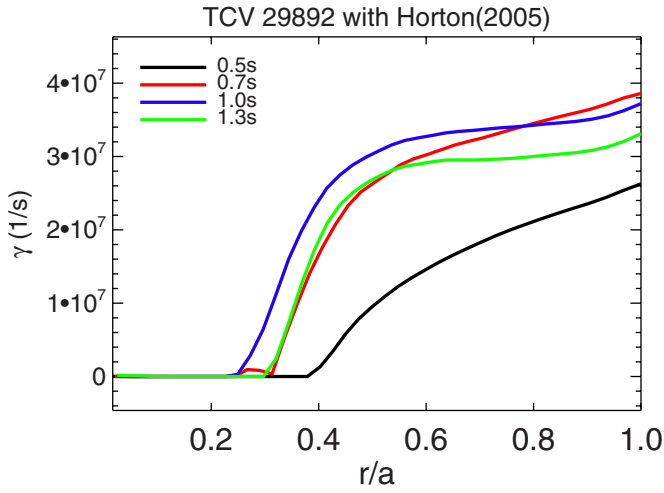
FIG. 8. (Color online) The ETG mode growth rates $\chi_{ETG}$ from Ref. 12.

$$\hat{N}_2 = \hat{N}_{212} + \hat{N}_{221} + \hat{N}_{223} = -[\phi, \nabla_\perp^2 A_\parallel] - \frac{\beta_e}{2}[A_\parallel, \phi - \delta T_e],$$

$$\hat{N}_3 = \hat{N}_{313} + \hat{N}_{322} = -[\phi, \delta T_e] + (\Gamma - 1)\frac{\beta_e}{2}[A_\parallel, \nabla_\perp^2 A_\parallel],$$

where the Poisson bracket $[f, g] = (\partial f / \partial x)(\partial g / \partial y) - (\partial g / \partial x)$ $\times (\partial g / \partial x)$.

The energy equations without viscosity, resistivity and diffusion become

$$\frac{\partial W_E}{\partial t} = \langle \phi \hat{L}_{11} \phi \rangle + \langle \phi \hat{L}_{12} A_\parallel \rangle + \langle \phi \hat{L}_{13} \delta T_e \rangle - \langle \phi \hat{N}_{122} \rangle$$

$$= \left\langle \phi \nabla_\perp^2 \frac{\partial A_\parallel}{\partial z} \right\rangle + 2\epsilon_n \left\langle \phi \frac{\partial \delta T_e}{\partial y} \right\rangle - \frac{\beta_e}{2} \langle \phi [A_\parallel, \nabla_\perp^2 A_\parallel] \rangle,$$

$$\frac{\partial W_B}{\partial t} = -\langle \nabla_\perp^2 A_\parallel \hat{L}_{21} \phi \rangle - \langle \nabla_\perp^2 A_\parallel \hat{L}_{22} A_\parallel \rangle - \langle \nabla_\perp^2 A_\parallel \hat{L}_{23} \delta T_e \rangle$$

$$+ \langle \nabla_\perp^2 A_\parallel (\hat{N}_{221} + \hat{N}_{223}) \rangle$$

$$= -\left\langle \phi \nabla_\perp^2 \frac{\partial A_\parallel}{\partial z} \right\rangle + \left\langle \delta T_e \nabla_\perp^2 \frac{\partial A_\parallel}{\partial z} \right\rangle$$

$$+ \frac{\beta_e}{2} \langle \phi [A_\parallel, \nabla^2 A_\parallel] \rangle - \frac{\beta_e}{2} \langle \delta T_e [A_\parallel, \nabla^2 A_\parallel] \rangle,$$

$$\frac{\partial W_{\delta T_e}}{\partial t} = \frac{1}{\Gamma - 1} (-\langle \delta T_e \hat{L}_{31} \phi \rangle - \langle \delta T_e \hat{L}_{32} A_\parallel \rangle - \langle \delta T_e \hat{L}_{33} \delta T_e \rangle$$

$$+ \langle \delta T_e \hat{N}_{322} \rangle)$$

$$= \left(\frac{\eta_e}{\Gamma - 1} - 4\epsilon_n\right) \left\langle \phi \frac{\partial \delta T_e}{\partial y} \right\rangle - \left\langle \delta T_e \nabla_\perp^2 \frac{\partial A_\parallel}{\partial z} \right\rangle$$

$$+ \frac{\beta_e}{2} \langle \delta T_e [A_\parallel, \nabla_\perp^2 A_\parallel] \rangle,$$

where

$$W_E = \frac{1}{2} \langle \tau |\phi|^2 + |\nabla_\perp \phi|^2 \rangle,$$

$$W_B = \frac{1}{2} \left\langle \frac{\beta_e}{2} |\nabla_\perp A_\parallel|^2 + |\nabla_\perp^2 A_\parallel|^2 \right\rangle,$$

$$W_{\delta T_e} = \frac{1}{2(\Gamma - 1)} \langle |\delta T_e|^2 \rangle,$$

and the integration $\langle \cdot \rangle$ is done over $dxdy$. The total energy evolves as

$$\frac{\partial}{\partial t}(W_E + W_B + W_{\delta T_e}) = -\left(\frac{\eta_e}{\Gamma - 1} - 4\epsilon_n\right) \left\langle \delta T_e \frac{\partial \phi}{\partial y} \right\rangle$$

$$- \left\langle \sqrt{\frac{8}{\pi}} |k_\parallel| |\delta T_e|^2 \right\rangle. \quad (13)$$

$E \times B$ induced turbulent energy, $\langle \delta T_e \partial \phi / \partial y \rangle$, determines the total energy evolution.

The linear stability analysis of the fluid model shows the large increase of the linear growth rates from $t = 0.5$ s to 0.7 s (Fig. 8). In the inner region $r/a < 0.3$ the mode is almost completely stabilized. The strong ETG instabilities at the later times are consistent with the behavior of the heat diffusivities estimated from the power balance analysis.

The full nonlinear simulations in Fig. 9(a) for $r/a = 0.7$ reveal that the electron heat fluxes are overestimated by a factor of 2 with the Landau damping term but the simulations agree with the sharp increase of the electron heat fluxes observed between the Ohmic phase and the later phases and comparable heat fluxes during the later phases. The errors are the standard deviation at the nonlinear stage of the simulation. At the nonlinear stage of the simulation, the vortices and radially extended structures with size of $10 - 20\rho_e$ are produced, see Fig. 9(b).

### B. Estimation of the importance of the ETG transport

As the nonlinear simulations are too heavy numerically to give the heat transport over the whole minor radius, we use a scaling law to estimate ETG driven transport in the discharge. The gyro-Bohm-type heat diffusivities with length scale $q\rho_e$ and time scale $L_{T_e}/v_{T_e}$,[25] is

$$\chi_e = \alpha_{ETG} q^2 \rho_e^2 v_{T_e} \left(\frac{1}{L_{T_e}} - \frac{1}{L_{T_c}}\right), \quad (14)$$

where $q$ is the safety factor and $\alpha_{ETG}$ is a scaling coefficient obtained from comparison with experimental data or with more rigorous theoretical calculations.

In the region $r/a > 0.4$, we calculated $\chi_e$ in Eq. (14) using the inverse of the critical length, $1/L_{T_c} = (1 + Z_{eff}T_e/T_i)(1.33 + 1.9|s|/q)/R$.[25] The critical temperature length turns out to be five to ten times larger than the inferred electron temperature gradient length, $L_{T_e}$ at $r/a > 0.4$.

The average relative variance (ARV) (Refs. 18 and 19) is the degree to which the theoretical models explain the power balance and is given in terms of

(a) Electron heat fluxes.
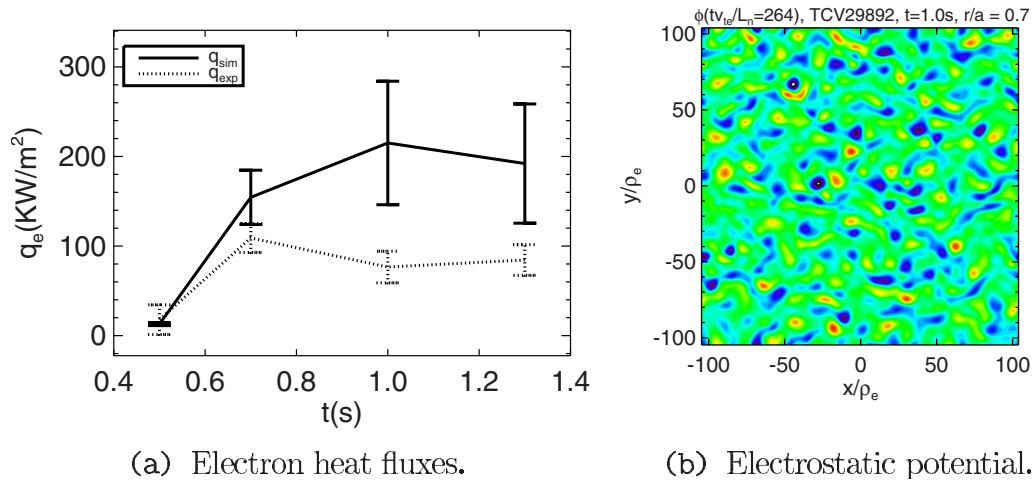


(b) Electrostatic potential.

FIG. 9. (Color online) Electron heat fluxes (a) from nonlinear ETG fluid simulations. The solid and dashed lines represent the simulations and the experiment, respectively. The contours of electrostatic potential $\phi(x, y)$ (b) from the nonlinear simulation at TCV29892 $r/a=0.7$ and $t=1.0$ s, where $\rho_e=75$ $\mu$m and the box corresponds to 1.5 cm×1.5 cm.

$$\mathrm{ARV}_j = \frac{\Sigma_i (\chi_{e,i} - \chi_i^{pb})^2}{\Sigma_i (\chi_i^{pb} - \langle \chi_i^{pb} \rangle)^2}, \tag{15}$$

with the spatial and temporal indices $i$ and $j$, respectively, of TCV 29892, the power balance diffusivities $\chi_i^{pb}$ and the heat diffusivity $\chi_{e,i}$ from Eq. (14). Here $\langle \chi_i^{pb} \rangle$ is the average power balance diffusivity over all radial points for each temporal index $j$. For each temporal index $j$, there is a total of 41 points whereof there are 30 radial points for $r/a > 0.4$. The ARV is a good measurement for indicating how well a model's prediction follows the behavior of the reference experiments. When the averages of $\chi_{e,i}$ and $\chi_i^{pb}$ are comparable, ARV $<1$ indicates that a model behaves in the same way as the experiment as shown in Fig. 10 where $\chi_i^{pb}$ increases as $\chi_e^{ETG}$. A smaller ARV means better agreement.

The model with $\alpha_{ETG} \sim 0.8$ shows the best agreement beyond $r/a=0.4$ in Fig. 10. The gyro-Bohm ETG heat diffusivity formula with a free parameter $\alpha_{ETG}$, Eq. (14), explains not only the electron heat diffusivity increase with the H-mode transition but also gives ARV $\sim 0.3$ for $t=0.7$ s and 1.0 s. For $t=0.5$ s, the flat experimental heat flux profile gives a small numerator in Eq. (15) producing the large ARV. With $\alpha_{ETG} \sim 1$ and the assumption that the dominant time scale is $\omega \sim v_{T_e}/L_{T_e}$, we can estimate the correlation length $l_c \sim 2\pi q \rho_e \sim 10 \rho_e$, consistent with the nonlinear simulation result.

## IV. ION TEMPERATURE GRADIENT AND TRAPPED ELECTRON TRANSPORT

This section investigates the stability of and the transport produced by the ion temperature gradient (ITG) and the trapped electron (TEM) modes. An analytical model[6,7] as well as the Weiland model[8–11] will be used as tools to calculate the local stability of these modes.

### A. Analytical TEM-ITG drift-wave model

Without the ion-wave resonances, the dispersion relation with temperature and density gradient driven drift-waves ($\omega \sim \omega_* = k_y T_e/eBL_n$) is given as[6,7]

$$
\begin{aligned}
D(\boldsymbol{k}, \omega, \boldsymbol{P}) &= 1 + \frac{T_e}{T_i} - \left( \frac{T_e}{T_i} + \frac{\omega_*}{\omega} \right) \Gamma_0 - \eta_i \frac{\omega_*}{\omega} b_i (\Gamma_1 - \Gamma_0) \\
&\quad - \int_0^\infty 2\pi v^2 dv F_e^M(v) \int_{-1}^{+1} d\mu h_e(v, \mu, \omega) \\
&= 0,
\end{aligned}
\tag{16}
$$

where the perturbed electron phase-space distribution fraction is $\tilde{f} = (e\phi/T_e) F_e^M (1 - h_e)$ with $F_e^M(v)$ the Maxwell distribution for the electron velocity. Moreover, $\eta_{i,e} = d \log T_{i,e}/d \log n_{i,e}$ and the usual finite ion gyroradius
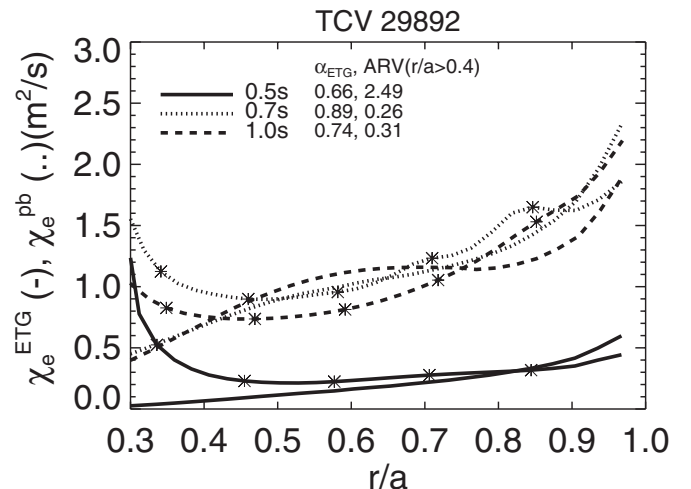


FIG. 10. The comparison between the electron gyro-Bohm heat diffusivity, $\chi_e$ in Eq. (14), with ETG time and spatial scales (lines with *) and the power balance heat diffusivity $\chi_e^{pb}$ (no mark) for each time slice $t=0.5$ (solid), 0.7 (dotted), and 1.0 (dashed) are shown.
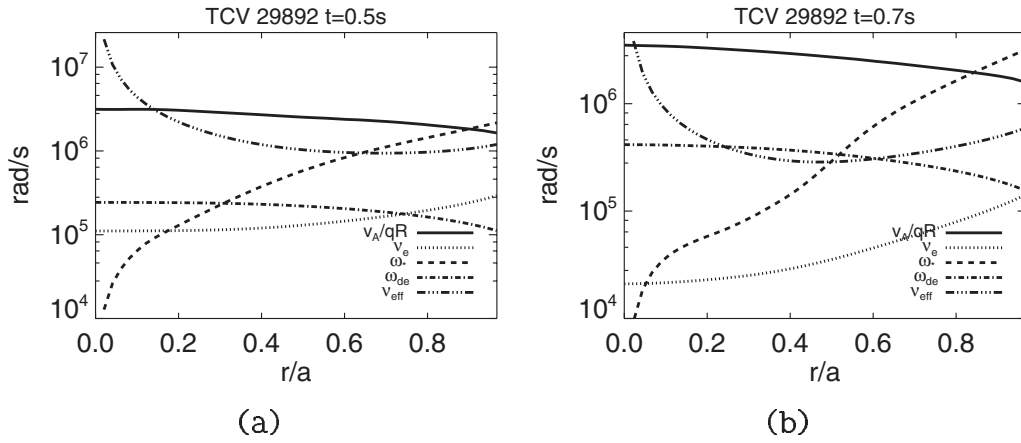
FIG. 11. Characteristic frequency profile of Alfvén transit frequency $V_A/qR$, electron collision frequency $\nu_e$, drift wave frequency $\omega_*(k_y\rho_s=1.0)$, magnetic drift frequency $\omega_{\mathrm{De}}(k_y\rho_s=1.0)$, and effective collision frequency $\nu_{\mathrm{eff}}=\nu_e/\epsilon$ for $t=0.5$ s in the Ohmic phase and 0.7 s in the ELMy H mode phase, TCV 29892.

Bessel function $\Gamma_n(b_i)=e^{-b_i}I_n(b_i)$ where $b_i=k_y^2\rho_i^2$. The nonadiabatic part of the electron distribution $h_e(v,\mu)$ satisfies the kinetic equation

$$\nu(v)\frac{\partial}{\partial\mu}(1-\mu^2)\frac{\partial h_e}{\partial\mu}+i\left[\omega-\omega_{\mathrm{De}}\frac{v^2}{v_e^2}-k_\parallel v\mu\right]h_e$$

$$=i\left[\omega-\omega_*\left[1+\eta_e\left(\frac{v^2}{v_e^2}-\frac{3}{2}\right)\right]\right],\tag{17}$$

where $\nu(v)=\nu_e(v_e/v)^3$, $\omega_{\mathrm{De}}\simeq\omega_*(2L_n/R)=2\omega_*\epsilon_n$, $\eta_e=d\log T_e/d\log n_e$, $v_e=(2T_e/m_e)^{1/2}$, and $\mu=v_\parallel/v$.

The model has the relevant electron temperature gradient and the density gradient as the primary driving forces for instability in this strongly heated plasma with no toroidal momentum input. The theoretical studies cited above of the ETG show that it is the key instability for producing a strong electron thermal turbulent transport without large particle transport. The instability is insensitive to the details of magnetic shear when the $q$ profile is monotonically increasing and the shear parameter $s<1$. In the case of hollow or inverted $q$-profiles, there occurs an electron transport barrier for reasons explained in Horton *et al.*[12]

The dispersion function $D(\boldsymbol{k},\omega,\boldsymbol{P})$ depends on the $d=8$ dimensional system parameter vector $\boldsymbol{P}$, which in dimensionless form is

$$\boldsymbol{P}=\left(\eta_i,\eta_e,\epsilon_n=\frac{L_n}{R},\epsilon=\frac{r}{R},q,\hat{s}=\frac{d\log q}{d\log r},\nu_*=\frac{\nu_e}{\epsilon\omega_{be}},\tau=\frac{T_e}{T_i}\right),\tag{18}$$

where $\omega_{be}^T=v_e\epsilon^{1/2}/L_c$ is the effective bounce frequency, $\epsilon=r/R$, $L_c=qR$ is the connection length. The reciprocal of the collisionality $\nu_*$ is the number of electron bounces before an effective (90°) detrapping collision. Thus, there is a large dimensional set of the response function, at least $2^8=256$ for high and low values of the eight parameters. Some of characteristic frequencies from the data is shown in Fig. 11 as a reference.

The perturbed electron distribution functions can be described with Legendre polynomials,[33]

$$h_e(v,\mu,\boldsymbol{k},\omega)=\Sigma_n h_{e,n}(v)P_n(\mu),\tag{19}$$

where in the zeroth order the pitch angle dependence is ignored. In the limiting case the functions can be divided into the following behaviors[34] depending on the electron energy:

(1) Low electron energies: The parallel electron motion is collision-dominated for

$$\frac{v}{v_e}\leqslant\left(\frac{\nu_e}{k_\parallel v_e}\right)^{1/4}\rightarrow h_{e_0}(v)=\frac{\omega-\omega_*[1+\eta_e(v^2/v_e^2-3/2)]}{\omega+i(k_\parallel^2 v_e^2/6\nu_e)(v/v_e)^5}.\tag{20}$$

(2) Intermediate electron energies: The electron Landau resonance is formed,

$$\left(\frac{\nu_e}{k_\parallel v_e}\right)^{1/4}<\frac{v}{v_e}$$

$$\leqslant\left(\frac{\nu_e}{k_\parallel v_e\epsilon^{3/2}}\right)^{1/4}\rightarrow h_{e_0}(v)$$

$$=\frac{-i\pi}{2}\frac{\omega-\omega_*[1+\eta_e(v^2/v_e^2-3/2)]}{|k_\parallel|v_e(v/v_e)}.\tag{21}$$

(3) High electron energies: The electrons divide into passing and trapped populations. The trapped electron response is bounce-averaged, such as $\bar{\phi}=(1/\tau)\oint ds/v_\parallel\phi(s)$,

$$\frac{v}{v_e}\geqslant\left(\frac{\nu_e}{k_\parallel v_e\epsilon^{3/2}}\right)^{1/4}\rightarrow h_{e_0}(v)$$

$$=\left(\frac{\epsilon}{2}\right)^{1/2}\frac{\omega-\omega_*[1+\eta_e(v^2/v_e^2-3/2)]}{\omega-\omega_{\mathrm{De}}v^2/v_e^2+i(\nu_e/\epsilon)(v_e/v)^3},\tag{22}$$

where the passing electron contribution averages to zero.

Substituting Eqs. (20)–(22) into Eq. (16) yields the dispersion relation

$$D_0(\boldsymbol{k}, \omega, \boldsymbol{P}) = 1 + \frac{T_e}{T_i} - \left(\frac{T_e}{T_i} + \frac{\omega_*}{\omega}\right)\Gamma_0 - \eta_i \frac{\omega_*}{\omega}b(\Gamma_1 - \Gamma_0)$$

$$- \sum_m^3 (\Delta h_m^0 + \eta_e h_m^1)$$

$$= 0, \qquad (23)$$

where $\omega = \omega_0 + i\gamma$, $\Delta = 1 - \omega/\omega_*$, and the dimensionless energy integral Green's functions are

$$h_1^n = -\frac{2}{\pi^{1/2}} \int_0^{t_1} \frac{dt\, t^{1/2} e^{-t}(t - 3/2)^n}{1 - \Delta + i(t/t_0)^{5/2}}, \qquad (24)$$

$$h_2^n = i\pi^{1/2} \frac{\omega_*}{|k_\parallel| v_e} \int_{t_1}^{t_2} dt\, e^{-t}\left(t - \frac{3}{2}\right)^n, \qquad (25)$$

$$h_3^n = -\left(\frac{\epsilon}{2}\right)^{1/2} \frac{2}{\pi^{1/2}} \int_{t_2}^{\infty} dt\, t^{1/2} \frac{e^{-t}(t - 3/2)^n}{1 - \Delta - \epsilon_n t + i(t_3/t)^{3/2}}, \qquad (26)$$

with

$$t_0 = \left(\frac{6\nu_e \omega_*}{k_\parallel^2 v_e^2}\right)^{2/5}, \quad t_1 = c_1 \left(\frac{\nu_e}{k_\parallel v_e}\right)^{1/2},$$

$$t_2 = c_2 \left(\frac{\nu_e}{k_\parallel v_e \epsilon^{3/2}}\right)^{1/2}, \quad t_3 = \left(\frac{\nu_e}{\epsilon \omega_*}\right)^{2/3}, \qquad (27)$$

$h_1^n$, $h_2^n$, and $h_3^n$ correspond to the collisional drift wave, the collisionless drifts wave and the trapped electron mode, respectively.

With the assumption of $\gamma/\omega_0 \ll 1$ and $h_e \ll 1$, the mode frequency $\omega_0$ and growth rate $\gamma$ are

$$\omega_0 = \omega_* \frac{[\Gamma_0 + \eta_i b_i(\Gamma_1 - \Gamma_0)]}{1 + (T_e/T_i)(1 - \Gamma_0)} \qquad (28)$$

and

$$\frac{\gamma \omega_*}{\omega_0^2}[\Gamma_0 + \eta_i b_i(\Gamma_1 - \Gamma_0)] = \Delta \sum_{m=1}^3 \text{Im } h_m^0 + \eta_e \sum_{m=1}^3 \text{Im } h_m^1, \qquad (29)$$

where

$$\Delta = 1 - \frac{\omega_0}{\omega_*}. \qquad (30)$$

Im $h_m^n$ for even $n$ are positive definite and determine the electron particle diffusivity $D$ and the heat diffusivity $\chi_e$. For odd $n$, Im $h_m^n$ are indefinite in sign. Also, the contribution of $\Delta h_m^0$ and $\eta_e h_m^1$ to the growth rates determines which is the more critical parameter between the density gradient and the temperature gradient.

We calculated the drift-waves and TEM modes at the radial position $r/a = 0.7$ at $t = 1.0$ s of TCV 29892, $(T_e, T_i) = (1.30, 0.76)$ keV, $n_e = 5.74 \cdot 10^{19}$ m$^{-3}$, $B_T = 1.09$ T, $\eta_e = 2.3$ and $\hat{s} = 0.65$. The relative plasma pressure is $\beta_e = 2\mu_0 p_e / B_T^2 = 0.025$ so that the $\omega \ll k_\parallel v_A$ and the modes are approximately electrostatic.
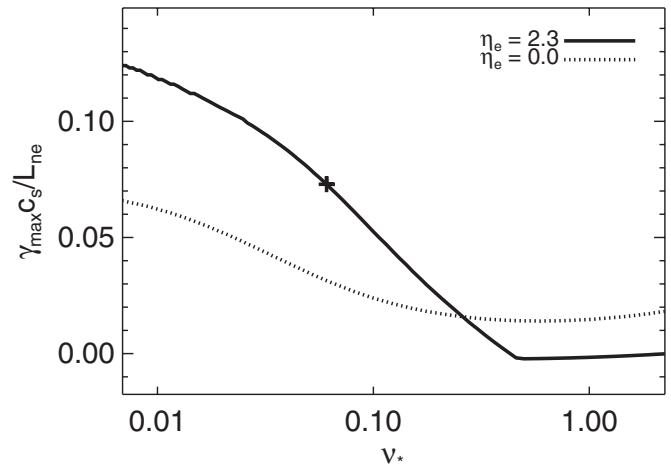


FIG. 12. The comparison of the maximum TEM growth rate vs the collisionality $\nu_*$ between the $\eta_e = 2.3$ (solid, data) and $\eta_e = 0$ (dotted). The variation of collisionality $\nu_*$ is obtained by varying $T_e = 200 - 3000$ eV and with the fixed temperature ratio $T_e/T_i$. The TCV data from $t = 1.0$ and $r/a = 0.7$ is marked with "+".

In Fig. 12 we compare the growth rates between the data case $\eta_e = 2.3$ (solid) and the reference case $\eta_e = 0$ (dotted) where in the absence of an electron temperature gradient, only the density gradient drives turbulence. It shows that the electron temperature gradient $\eta_e$ leads to the distinct transition around $\nu_* = 0.45$ between a low growth rate collisional drift wave mode and the high growth rate trapped electron mode. In the region for $\nu_* < 0.10$ including $\nu_* = 0.06$ from the profile (marked + in Fig. 12), the electron temperature gradient driven TEM instability is a factor two larger than the collisional drift wave instability driven by the electron density gradient. As far as the magnetic shear is concerned, the shear dynamics only plays a role in determining the parallel wavelength $k_\parallel L_n = k_y \rho_s \hat{s}^{1/2}$. Therefore collisional and collisionless drift waves are affected by the magnetic shear through collisional dissipation and Landau damping. So, the magnetic shear dynamics has little influence over the trapped electron mode in our model. The electron response functions for $\eta_e = 2.3$ and 0 with $\nu_* = 0.06$ of the experiment are com-
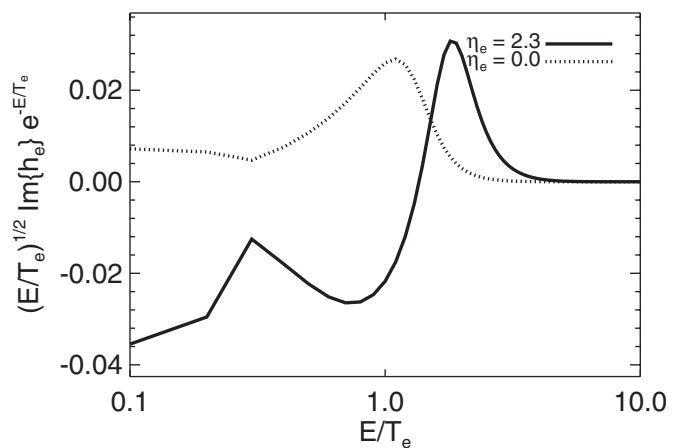


FIG. 13. The nonadiabatic TEM electron response functions of the data case $\eta_e = 2.3$ (solid) and the reference case $\eta_e = 0$ (dotted).
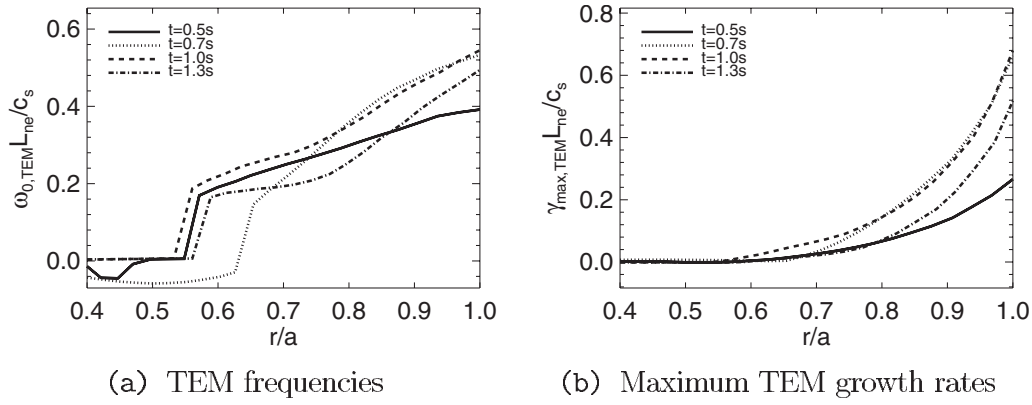
(a) TEM frequencies

(b) Maximum TEM growth rates

FIG. 14. The TEM mode frequencies and the maximum growth rates of TCV 29892 at $t=0.5$ (solid), 0.7 (dotted), 1.0 (dashed), and 1.3 s(dashed-dotted) obtained from Eq. (29). The maximum growth rate is obtained among the different $k_y$ values.

pared in Fig. 13. The wave/guiding-center drift resonances occur at $E/T_e \sim \omega_0/\omega_{De}$. With the temperature driven case $\eta_e=2.3$, the resonance shifts from $E/T_e=1.1$ to 1.9 and it is clearly seen that the temperature gradient term $\eta_e(E/T_e - 3/2)$ stabilizes the lower energy contribution ($E/T_e < 3/2$) to the TEM modes and destabilizes the higher energy contribution ($E/T_e > 3/2$) to the TEM modes.

For all time slices and for all the radial profiles, we calculate the mode frequency, growth rate, and electron response functions with the same procedure. The mode frequencies and the maximum growth rates for each radial point are shown at each time slice (Fig. 15). At $r/a=0.45-0.55$, there is a transition between drift waves and trapped electron modes. The drift waves propagate in the ion drift wave direction with low frequencies $\omega_0 \ll 0.1c_s/L_{ne}$ contrary to the

TEM modes with higher frequencies $\omega_0 \sim 0.1c_s/L_{ne}$ at $r/a \gtrsim 0.5$, which propagate in the electron drift wave direction.

For each time slice, the drift wave modes are weakly destabilized. Beyond the transition radial position $r/a=0.5$, the trapped electron mode is $\eta_e$-dominated and the temperature gradient stabilizes the drift wave mode. Towards the edge, the density and temperature gradients contribute to the instability with comparable magnitudes.

This method is based on $\omega \gg \gamma$ but in some cases, it is found that $\omega \simeq \gamma$. For further calculations, the mode frequencies and the growth rates will be calculated by an iteration method. This means that the nonadiabatic electron response function $h_e$ needs to be considered for the mode frequencies.

The imaginary parts of electron response function are shown in Fig. 16. In Eq. (29) a positive value of the product
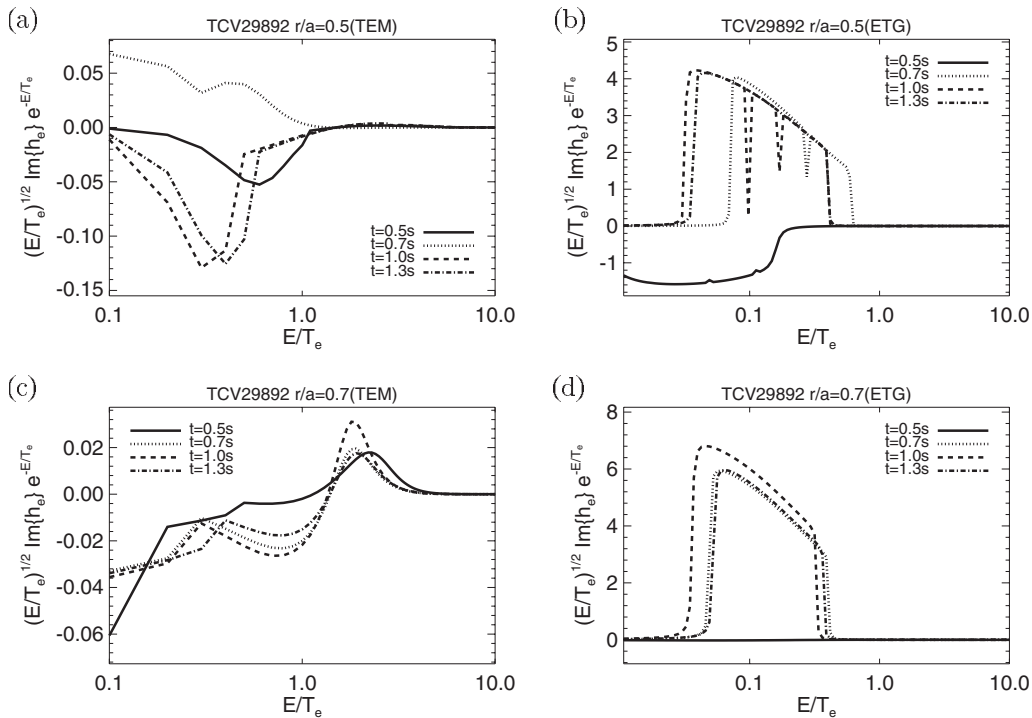


FIG. 15. The imaginary part of electron response functions at $r/a=0.5$ (top panels) and $r/a=0.7$ (bottom panels). The left and right panels are for TEM, Eqs. (20) and (21), and ETG, Eq. (7), respectively.
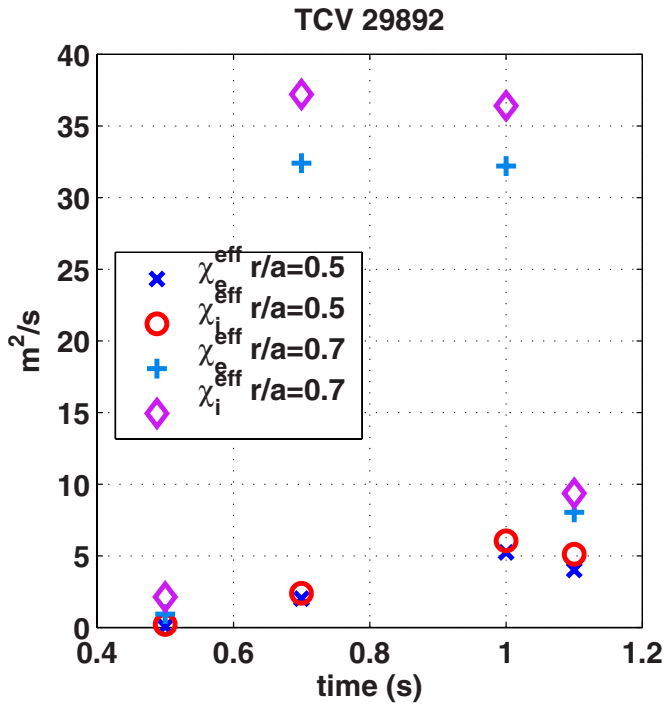
**TCV 29892**



FIG. 16. (Color online) Effective electron and ion diffusivities calculated by the local Weiland model at $r/a=0.5$ and 0.7.

of the response function and the sign of the mode frequency $\omega_0$ implies the destabilizing contribution of the trapped electrons. The sign of the functions are readjusted in order to indicate destabilizing contribution by positive values of the response function. At $r/a=0.5$ as in Figs. 15(a) and 15(b), for $t=0.5, 1.0, 1.3$ s, the collisionless and collisional drift waves are stabilized by the electron temperature gradient, while for $t=0.7$ s, the TEM/ITG mode propagates in the ion diamagnetic drift direction, $\omega_0<0$, due to the large ion temperature gradient $\eta_i=3$ and the electron temperature gradient drives the TEM instability for the lower energy $E/T_e<3/2$ and drift wave instability.

For $t=0.5$ s, the ETG mode propagates in the ion diamagnetic direction due to the small electron temperature gradient $\eta_e=1.5$ which stabilizes the ETG mode in the lower energy $E/T_e<3/2$ spectrum. At the later times, the ETG modes propagate in the electron diamagnetic direction

$\omega_0>0$ and the temperature gradient drives strong ETG instabilities. The ETG modes have the broad energy range of the resonances due to electron Landau damping $\omega_0-\omega_{\text{De}}E -k_{\parallel}v_{T_e}=0$ and strong resonances due to the lower collisional frequencies $\nu_e L_{n_e}/v_{T_e}\ll\nu_e L_{n_e}/c_s$ compared to the TEM modes.

At $r/a=0.7$ as in Figs. 15(c) and 15(d), for all the times, the electron temperature drives the TEM/ITG instabilities at the higher energy $E/T_e>3/2$ and stabilizes them at the lower energy as we have seen in Fig. 13. The competitive electron temperature gradient effects lead to the TEM instability in the end. The ETG modes are also destabilized by the temperature gradient at the lower energy. Nevertheless the high collisional frequency at $t=0.5$ s weakens the resonance and the ETG instability. The stronger resonances at later times are consistent with the power balance transport, Fig. 10.

## B. The Weiland model

The Weiland model[8–11,35–37] is normally used to predict the radial global transport. In this section it is used as a local stability tool to analyze the instabilities present in the plasma and their thresholds, and to calculate the local transport they generate. The version of the Weiland model used here includes electromagnetic effects, collisions, impurity and magnetic shear effects but neglects varying correlation length[38] and toroidal and poloidal rotation effects.[39,40] The two latter are included in a more refined version of the model.

Tables II–V show all unstable modes found by the local Weiland model at $r/a=0.5$ and $r/a=0.7$ for $t=0.5$ s, 0.7 s, 1.0 s, and 1.3 s, respectively. Several modes are present at each radius and this is reflected in the multiple rows of $\hat{\omega}_r$, $\hat{\gamma}$, $\chi_i$, and $\chi_e$ for each $r/a$. TEM and ITG modes are defined by $\hat{\omega}_r>0$ and $\hat{\omega}_r<0$, respectively. The two rightmost columns show the contributions of each instability to the ion and electron diffusivity. The contribution of each mode to $\chi_i$ or $\chi_e$ sums up to $\chi_i^{\text{eff}}$ or $\chi_e^{\text{eff}}$, respectively. If a contribution to $\chi_i$ or $\chi_e$ is negative, then this implies a heat pinch. Impurity ITG modes are marked with "a".

In principle, the TEM (ITG) mode mainly drives electron (ion) transport but the Weiland model (W) uses a sophisticated gyro-Bohm-type mixing-length formula,[41]

TABLE II. TEM ($\hat{\omega}_r>0$) and ITG ($\hat{\omega}_r<0$) modes present at $t=0.5$ s at two different radii.

| $r/a$ | $T_e/T_i$ | $R/L_{ne}$ | $R/L_{Te}$ | $R/L_{Ti}$ | $F_e$ | $F_i$ | $\chi_i^{\text{eff}}(\text{m}^2/\text{s})$ | $\chi_e^{\text{eff}}(\text{m}^2/\text{s})$ | $\hat{\omega}_r$ | $\hat{\gamma}$ | $\chi_i(\text{m}^2/\text{s})$ | $\chi_e(\text{m}^2/\text{s})$ |
|---|---|---|---|---|---|---|---|---|---|---|---|---|
| 0.5 | 1.35 | 2.69 | 4.14 | 2.65 | 1.24 | 0.92 | 0.204 | 0.045 | 1.84 | 0.039 | 0.013 | 0.047 |
|  |  |  |  |  |  |  |  |  | −1.08 | 0.13 | 0.19 | −0.002 |
| 0.7 | 1.22 | 6.15 | 7.60 | 5.53 | 0.54 | 0.44 | 2.13 | 0.93 | 0.78 | 0.10 | 0.25 | 0.97 |
|  |  |  |  |  |  |  |  |  | −0.48 | 0.23 | 1.61 | −0.003 |
|  |  |  |  |  |  |  |  |  | −0.14[a] | 0.14 | 0.26 | −0.030 |

[a]Impurity ITG.

TABLE III. TEM ($\hat{\omega}_r > 0$) and ITG ($\hat{\omega}_r < 0$) modes present at $t = 0.7$ s at two different radii.

| $r/a$ | $T_e/T_i$ | $R/L_{ne}$ | $R/L_{Te}$ | $R/L_{Ti}$ | $F_e$ | $F_i$ | $\chi_i^{\text{eff}}(\text{m}^2/\text{s})$ | $\chi_e^{\text{eff}}(\text{m}^2/\text{s})$ | $\hat{\omega}_r$ | $\hat{\gamma}$ | $\chi_i(\text{m}^2/\text{s})$ | $\chi_e(\text{m}^2/\text{s})$ |
|---|---|---|---|---|---|---|---|---|---|---|---|---|
| 0.5 | 2.08 | 0.92 | 6.25 | 2.71 | 3.62 | 1.74 | 2.39 | 2.01 | 5.18 | 0.71 | 1.49 | 1.97 |
|  |  |  |  |  |  |  |  |  | 1.86 | 0.36 | −0.012 | 0.038 |
|  |  |  |  |  |  |  |  |  | −1.80 | 0.15 | 0.90 | 0.001 |
| 0.7 | 1.68 | 4.06 | 9.44 | 5.64 | 0.82 | 0.49 | 37.2 | 32.4 | 0.78 | 1.49 | 30.8 | 28.4 |
|  |  |  |  |  |  |  |  |  | 0.64 | 0.47 | 3.09 | 3.75 |
|  |  |  |  |  |  |  |  |  | −0.20[a] | 0.15 | 3.33 | 0.26 |

[a]Impurity ITG.

$$\chi_{e,i}^{\text{W}} = \frac{R/L_{Te,i} - p(\hat{\omega}_{re,i}, L_n)}{R/L_{Te,i}}$$
$$\times \left\{ f_{e,i} \frac{m_i^{1/2}}{k_\theta \rho_s e^2 B^2 L_{ne}} T_e^{3/2}(\text{eV}) \sum_{\gamma > 0} \frac{\hat{\gamma}^3}{(\hat{\omega}_r \mp F_{e,i})^2 + \hat{\gamma}^2} \right\},$$

(31)

where

$$F_{e,i} = \frac{10}{3} \frac{L_{ne}}{R} \frac{T_{e,i}}{T_e}.$$

(32)

Above $e$ and $i$ denote electron and ion, respectively. Here $f_e = f_t$, is the trapped electron fraction and $f_i = 1$. The mode frequency, $\hat{\omega}_r$, and growth rate, $\hat{\gamma}$, are normalized to the diamagnetic drift frequency of the electrons ($\omega_* = k_\theta \rho_s c_s / L_{ne}$). It is also assumed that the radial correlation length is of the same order as the poloidal one, i.e., $k_r^2 \approx k_\theta^2$. A heat pinch arises in Eq. (31) when the threshold function $p(\hat{\omega}_{re,i}, L_n)$ is larger than $R/L_{Te,i}$, thus making $\chi_{e,i}$ negative. For this discharge all the net $\chi_e$ and $\chi_i$ are positive from the Weiland model as shown in Tables II–V. The part of Eq. (31) within the curly brackets gives the mixing length diffusivity.

In Eq. (31), the sum over $\gamma$ is over all unstable modes. Hence, TEM modes can drive ion transport and ITG modes electron transport depending on the relative sizes of the resonance factor, ($\hat{\omega}_r \mp F_{e,i}$), and the growth rate. In the case of ion transport, the resonance factor will decrease with $F_i$ if both $R/L_{ne}$ and $T_e/T_i$ are much larger than unity. In such a case, a significant TEM drive of $\chi_i$ can be expected.[42]

In Fig. 16 the trend of the diffusivities at $r/a = 0.7$ agrees with the trend of the experimental heat fluxes shown in Fig. 9 up to $t = 1.0$ s. At $t = 1.3$ s the MHD activity reduces the gradients in the outer part of the plasma, which results in a marked drop in the diffusivities at $r/a = 0.7$. This drop was also seen in the nonlinear ETG simulations for the same reason.

The diffusivities in Fig. 16 for $r/a = 0.5$ follows the same trend as for $r/a = 0.7$ with the exceptions that between $t = 1.0$ s and 1.3 s the diffusion only gets smaller by 20% and that the diffusivities at 0.7 s are not of the same magnitude as at 1.0 s. The latter can be explained by the resonance factor, ($\hat{\omega}_r \mp F_{e,i}$) in Eq. (31).

Tables III and IV show that the TEM instabilities dominate both ion and electron transport. Moreover, for $r/a = 0.5$ the TEM growth rate at 1.0 s is smaller than at 0.7 s but it still drives a factor of 2.5 (electron)–4 (ion) more transport than is produced at 0.7 s. As the temperatures and their gradient length scales are comparable in the two cases, the difference in behavior can be pinned down to the density gradient length scale. The latter reduces the transport at 0.7 s as the sum in Eq. (31) is multiplied by $1/L_{ne}$ but also by increasing the resonance factor in two ways. First, as $\hat{\omega}_r$ increases with smaller $R/L_{ne}$,[11,43] it doubles at 0.7 s compared with 1.0 s (at $r/a = 0.5$). Secondly it decreases the factor $F_i$ ($F_e$) from 1.74 (3.62) at 0.7 s to 0.75 (1.62) at 1.0 s. This implies that ($\hat{\omega}_r \mp F_{e,i}$)$^2$ will be up to a factor of 5 bigger at 0.7 s compared with 1.0 s. The larger growth rate at 0.7 s reduces the effect of the resonance factor. Hence, at $r/a = 0.5$, $1/L_{ne} \cdot \hat{\gamma}^3 / [(\hat{\omega}_r \mp F_{e,i})^2 + \hat{\gamma}^2]$ predicts five times smaller transport at 0.7 s than at 1.0 s for the ions and three times smaller for the electrons. These numbers are slightly larger than what direct comparisons of the diffusivities give, but it clearly demonstrates the impact of the lower $R/L_{ne}$ at $r/a = 0.5$ for 0.7 s.

During the Ohmic phase at $t = 0.5$ s (see Table II), the transport is much lower than in the following ECRH heated

TABLE IV. TEM ($\hat{\omega}_r > 0$) and ITG ($\hat{\omega}_r < 0$) modes present at $t = 1.0$ s at two different radii.

| $r/a$ | $T_e/T_i$ | $R/L_{ne}$ | $R/L_{Te}$ | $R/L_{Ti}$ | $F_e$ | $F_i$ | $\chi_i^{\text{eff}}(\text{m}^2/\text{s})$ | $\chi_e^{\text{eff}}(\text{m}^2/\text{s})$ | $\hat{\omega}_r$ | $\hat{\gamma}$ | $\chi_i(\text{m}^2/\text{s})$ | $\chi_e(\text{m}^2/\text{s})$ |
|---|---|---|---|---|---|---|---|---|---|---|---|---|
| 0.5 | 2.15 | 2.06 | 6.26 | 2.44 | 1.62 | 0.75 | 6.05 | 5.24 | 2.35 | 0.54 | 5.97 | 5.16 |
|  |  |  |  |  |  |  |  |  | 0.84 | 0.25 | 0.076 | 0.080 |
|  |  |  |  |  |  |  |  |  | −1.55 | 0.024 | −0.001 | 0.00 |
| 0.7 | 1.70 | 4.24 | 9.71 | 5.81 | 0.79 | 0.46 | 36.4 | 32.2 | 0.87 | 1.45 | 31.7 | 30.8 |
|  |  |  |  |  |  |  |  |  | 0.54 | 0.29 | 0.97 | 1.08 |
|  |  |  |  |  |  |  |  |  | −0.45 | 0.34 | 3.69 | 0.32 |

TABLE V. TEM ($\hat{\omega}_r > 0$) and ITG ($\hat{\omega}_r < 0$) modes present at $t = 1.3$ s at two different radii.

| $r/a$ | $T_e/T_i$ | $R/L_{ne}$ | $R/L_{Te}$ | $R/L_{Ti}$ | $F_e$ | $F_i$ | $\chi_i^{\text{eff}}$(m$^2$/s) | $\chi_e^{\text{eff}}$(m$^2$/s) | $\hat{\omega}_r$ | $\hat{\gamma}$ | $\chi_i$(m$^2$/s) | $\chi_e$(m$^2$/s) |
|---|---|---|---|---|---|---|---|---|---|---|---|---|
| 0.5 | 1.83 | 2.04 | 6.13 | 1.99 | 1.63 | 0.89 | 5.11 | 4.01 | 2.48 | 0.50 | 5.03 | 3.98 |
|  |  |  |  |  |  |  |  |  | 0.88 | 0.21 | 0.079 | 0.029 |
| 0.7 | 1.39 | 3.42 | 8.50 | 4.10 | 0.9 | 0.70 | 9.36 | 8.04 | 1.20 | 0.55 | 4.57 | 6.35 |
|  |  |  |  |  |  |  |  |  | −1.08 | 0.63 | 2.32 | 0.51 |
|  |  |  |  |  |  |  |  |  | 0.25[a] | 0.54 | 2.46 | 1.18 |

[a]The code identifies this mode as an impurity ITG despite its positive frequency.

phases (Tables III–V), as the Ohmic heating of 0.49 MW is much smaller than the total heating with ECRH, $P_{\text{tot}} \sim 1.2$ MW. This Ohmic phase is also the only phase in which the ITG instability is at least twice as big as the TEM. As a consequence, the ITG modes drive most of the ion transport and the TEM most of the electron. In the following phases the TEMs dominate both ion and electron transport, even if the ITGs may give significant contributions to $\chi_i$.

In summary, according to the local Weiland model, the transport in TCV discharge 29892 is mainly driven by trapped electron modes in the ECRH heated phases for $t > 0.6$ s. At earlier times, TEM and ITG drive $\chi_e$ and $\chi_i$, respectively, as normally expected. Furthermore, as the electron heat diffusivities are much higher than those from the power-balance calculations, the ARV factor introduced in Eq. (15) is much larger than 1. An error analysis shows that the diffusivities can be reduced by, on average, ~75% for the ions and ~65% for the electrons by decreasing all gradients ($R/L_{ne}$, $R/L_{Te}$, and $R/L_{Ti}$) by 30%, which is within the error bars of the gradients. This would give diffusivities of similar magnitude to the experiment in inner part of the plasma, whereas further out they would still be overestimated. The local version of the Weiland model hence gives a poor quantitative picture of the heat transport. However, the TEM dominance remains even when decreasing the gradients and hence the qualitative analysis remains valid. The local version can therefore give a good idea of which modes are present and how the transport behaves qualitatively. For good qualitative and quantitative results, global predictive simulations with the Weiland model are needed and these will be presented in a separate publication.

## V. CONCLUSIONS

A high power heated discharge in the TCV tokamak is analyzed for the turbulent electron transport. Both the large space scale TEM-ITG modes and the small scale ETG modes are analyzed for the four phases of one TCV discharge 29892. The discharge is characterized by central power deposition into the electrons of about 5–8 MW/m$^3$ from third harmonic electron cyclotron heating and no direct additional ion heating. The discharge has four distinct phases: (1) the initial Ohmic phase with type III ELMs, (2) the type I ELMy H-mode phase after the turn-on of the 1.35 MW of third harmonic electron cyclotron heating, (3) the ELM-free H-mode phase, and (4) the final stage of an ELM-free plasma

with internal magnetic islands after a single ELM event where now the energy confinement time has dropped by about 15% below that in stage 3.

The ECRH deposits the power in the core of the discharge and thus there is a well defined flow of thermal energy through the electrons from the core plasma with $1 < T_e < 3$ keV to the edge plasma. This power flow allows to obtain a good estimate of the radial electron thermal flux $q_e$. With the associated accurately measured $T_e$ profiles, there is a well defined measure of the electron thermal diffusivity $\chi_e$. One uncertainty in $q_e$ and $\chi_e$ is from the lack of a measured $T_i$ profile, which would allow precise calculation of the collisional transfer of electron power to the ions. We bracket this uncertainty by considering the variation of $q_e$ between the values computed with a low $T_i \sim 1/3 T_e(r)$ and with a high $T_i$ that is close to $T_e$ where then the power transfer term $P_{e \rightarrow i}$ is negligible. The range of the error of $q_e$ is then found to be at most 10% in the ECRH-heated cases, but can be considerably higher in the Ohmic phase. The differences in the theoretical models for $q_e$ are considerably larger than this uncertainty, which allows us to draw some conclusions.

We report that the analytical TEM/ITG mode transport formulas have difficulty in explaining both the magnitude and radial profile of the electron thermal flux. Depending on the collisionality regime the TEM mode is either driven by the electron temperature gradient or by the density gradient. In some regimes, increasing the grad $T_e$ has little effect or even reduces the TEM growth as it does for the slab electron drift wave instability. The nonadiabatic trapped electron response function $h(\omega, k_y, \boldsymbol{P})$ is computed in detail. The TEM response function is shown to be relatively small and to have sharp resonances in its energy dependence. In contrast, the ETG turbulence is directly driven by the electron temperature gradient and both the trapped and passing electrons contribute to the instability and turbulent thermal flux. It is shown that there is a larger value of the out-of-phase component of the electron response function without sharp resonances in its energy spectrum. This difference makes the ETG formulas more broadly applicable to the wide range in the plasma stability parameter vector $\boldsymbol{P}$ for the range of $[r_i, t_j]$ values used in the transport analysis.

The nonlinear state of the ETG flux is calculated through turbulent simulations based on the three coupled gyrofluid partial differential equations whose linear modes describe well the ETG instability. The simulations show that the small scale fluctuations created at the maximum linear growth rate

undergo an inverse cascade to form large scale vortices and streamers. The correlation length for these large scale ETG structures reaches $l_c \sim (3-6)q\rho_e$. The resulting thermal diffusivity is sufficiently large and has a scaling to explain well the power balance data (Fig. 9).

We analyze and compare the ETG with the TEM-ITG formulas of Weiland and of Horton/IFS (Ref. 44) simplified local TEM-ITG transport formulas. To compare the results of the two models, we introduce the dimensionless error measure called the average relative variance, ARV, to quantitatively measure how much of the variation of the power balance $\chi_e$ is explained by the theoretical models.

For the simplified ETG model we show that the ARV is about 0.3, meaning that the model explains 70% of the variation of the electron diffusivity $\chi_e(r,t)$ inferred from power balance heat flux and the measured $T_e$ profile. For the TEM-ITG model we find that the ARV is above unity, ARV $\sim 1.3$. Also the local version of the Weiland model has ARV $>1$, which means that the quantitative prediction of the models are relatively poor since an ARV$=1$ is equivalent to taking average value of the data as the prediction model.

Although the magnitudes of the local Weiland diffusivities overestimate the power balance diffusivities, the trend follows that of the power balance diffusivities in the first three phases in the part of the plasma not affected by MHD activity. In the fourth phase a sharp decrease of the diffusivities can be seen, as well as for the nonlinear ETG heat fluxes, due to the lower gradients caused by the MHD activity. By decreasing the gradients within the error bars, the Weiland diffusivities may approach the experimental values. The main conclusion from the analysis with the local Weiland model, valid for both large and small gradients, is that the TEMs drive not only some of the total electron transport but are also responsible for the ion transport in the X3 heated H-modes.

In the ARV comparisons, we make a data set composed of the product of the 4 time slices and 41 radial points. Thus we conclude that the ETG model does substantially better at predicting the turbulent electron thermal flux in these high power density H-mode plasmas. These results for TCV help to validate the conclusion that the ETG model is capable of explaining a wide range of anomalous electron thermal transport data adding to the evidence from ASDEX,[14,15] Tore Supra by Hoang *et al.*,[16] and the Frascati Tokamak Upgrade.[17]

In future work, we plan to expand the TCV data base with more discharges and consider the use of the GyroKineticVlasov (GKV) code[45] in addition to the electron gyrofluid code used in this work. To further validate the ETG model we suggest a future experiment with variable ion masses including helium and argon, and the use of cross-polarization scattering to monitor the change in the small-scale magnetic fluctuation associated with ETG turbulence.

## ACKNOWLEDGMENTS

[1] G. Tonetti, A. Heym, F. Hofmann, C. Hollenstein, J. Koechili, K. Lahlou, J. B. Lister, Ph. Marmillod, J. M. Mayor, J. C. Magnin, F. Marcus, and R. Rage, in *Proceedings of the 16th Symposium on Fusion Technology, London, U.K.*, edited by R. Hemsworth (North-Holland, Amsterdam, 1991), p. 587.

[2] L. Porte, S. Coda, S. Alberti, G. Arnoux, P. Blanchard, A. Bortolon, A. Fasoli, T. P. Goodman, I. Klimanov, Y. Martin, M. Maslov, A. Scarabosio, and H. Weisen, in *21st IAEA Fusion Energy Conference* (IAEA, Vienna, 2006), pp. EX/P6-20.

[3] J. Lohr, B. W. Stallard, R. Prater, R. T. Snider, K. H. Burrell, R. J. Groebner, D. N. Hill, K. Matsuda, C. P. Moeller, T. W. Petrie, H. St. John, and T. S. Taylor, Phys. Rev. Lett. **60**, 2630 (1988).

[4] S. J. Fielding, J. D. Ashall, P. G. Carolan, A. Colton, D. Gates, J. Hugill, A. W. Morris, M. Valovic, and the COMPASS-D and ECRH Teams, Plasma Phys. Controlled Fusion **38**, 1091 (1996).

[5] K. Matsuda, IEEE Trans. Plasma Sci. **17**, 6 (1989).

[6] P. Zhu, W. Horton, and H. Sugama, Phys. Plasmas **6**, 2503 (1999).

[7] P. Zhu, G. Bateman, A. H. Kritz, and W. Horton, Phys. Plasmas **7**, 2898 (2000).

[8] S. Guo and J. Weiland, Nucl. Fusion **37**, 1095 (1997).

[9] A. Jarmén, P. Andersson, and J. Weiland, Nucl. Fusion **27**, 941 (1987).

[10] H. Nordman, J. Weiland, and A. Jarmén, Nucl. Fusion **30**, 983 (1990).

[11] J. Weiland, *Collective Modes in Inhomogeneous Plasma* (IOP, New York, 2000).

[12] W. Horton, H. V. Wong, P. J. Morrison, A. Wurm, J. H. Kim, J. C. Perez, J. Pratt, G. T. Hoang, B. P. LeBlanc, and R. Ball, Nucl. Fusion **45**, 976 (2005).

[13] J.-H. Kim, Ph.D. thesis, University of Texas at Austin (2008).

[14] F. Ryter, F. Leuterer, G. Pereverzev, H.-U. Fahrbach, J. Stober, W. Suttrop, and ASDEX Upgrade Team, Phys. Rev. Lett. **86**, 2325 (2001).

[15] F. Ryter, F. Imbeaux, F. Leuterer, H.-U. Fahrbach, W. Suttrop, and ASDEX Upgrade Team, Phys. Rev. Lett. **86**, 5498 (2001).

[16] G. T. Hoang, W. Horton, C. Bourdelle, B. Hu, X. Garbet, and M. Ottaviani, Phys. Plasmas **10**, 405 (2003).

[17] A. Jacchia, F. D. Luca, S. Cirant, C. Sozzi, G. Bracco, A. Brushi, P. Buratti, S. Podda, and O. Tudisco, Nucl. Fusion **42**, 1116 (2002).

[18] A. S. Weigend, B. A. Huberman, and D. E. Rumelhart, Int. J. Neural Syst. **1**, 193 (1990).

[19] T. Detman and D. Vassiliadis, in *Geophysical Monograph* (American Geophysical Union, New York, 1997), Vol. 98.

[20] A. N. Karpushov, B. P. Duval, C. Schlatter, V. I. Afanasyev, and F. V. Chernyshev, Phys. Plasmas **13**, 033503 (2006).

[21] G. Turri, O. Sauter, L. Porte, S. Alberti, E. Asp, T. Goodman, Y. Martin, V. Udintsev, and C. Zucca, J. Phys. A **39**, 6 (2008).

[22] Z. Chang and J. Callen, Nucl. Fusion **30**, 219 (1990).

[23] S. Hamaguchi and W. Horton, Phys. Fluids B **4**, 319 (1992).

[24] H. Sugama and W. Horton, Phys. Plasmas **2**, 2989 (1995).

[25] W. Horton, G. T. Hoang, C. Bourdelle, X. Garbet, M. Ottaviani, and L. Colas, Phys. Plasmas **11**, 2600 (2004).

[26] W. Horton and T. Tajima, J. Geophys. Res. **93**, 2741, DOI: 10.1029/JA093iA04p02741 (1988).

[27] J. Li and Y. Kishimoto, Phys. Plasmas **11**, 1493 (2004).

[28] C. Holland and P. H. Diamond, Phys. Plasmas **9**, 3857 (2002).

[29] W. Horton, B. G. Hong, and W. M. Tang, Phys. Fluids **31**, 2971 (1988).

[30] W. Horton, N. Bekki, H. L. Berk, B. G. Hong, M. J. LeBron, S. Mahajan, T. Tajima, and Y. Z. Zhang, in *12th International Conference on Plasma Physics and Controlled Nuclear Fusion Research* (International Atomic Energy Agency, London, 1988), cN-50/D-4-3.

[31] W. Horton, B.-G. Hong, T. Tajima, and N. Bekki, Comments Plasma Phys. Controlled Fusion **13**, 207 (1990).

[32] G. W. Hammett and F. W. Perkins, Phys. Rev. Lett. **64**, 3019 (1990).

[33] R. Koch and W. Horton, Phys. Fluids **18**, 861 (1975).

[34] W. Horton, Phys. Fluids **19**, 711 (1976).

[35] H. Nordman, P. Strand, A. Eriksson, and J. Weiland, Plasma Phys. Controlled Fusion **47**, L11 (2005).

[36] J. Weiland, E. Asp, X. Garbet, P. Mantica, V. Parail, P. Thomas, W. Suttrop, T. Tala, and the EFDA-JET Contributors, Plasma Phys. Controlled Fusion **47**, 441 (2005).

[37] H. Nordman, T. Fulop, J. Candy, P. Strand, and J. Weiland, Phys. Plasmas **14**, 052303 (2007).

[38]J. Weiland and I. Holod, Phys. Plasmas **12**, 012505 (2005).

[39]J. Weiland and H. Nordman, in Anomalous momentum transport due to drift waves in tokamaks, *33rd European Physical Society Conference on Plasma Physics*, Rome, Italy, 19–23 June, 2006, edited by F. De Marco and G. Vlad (European Physical Society, Rome, Italy, 2006), Vol. 31, p. P2.186.

[40]A. Eriksson, H. Nordman, P. Strand, J. Weiland, T. Tala, E. Asp, G. Corrigan, C. Giroud, M. de Greef, I. Jenkins, H. C. M. Knoops, P. Mantica, K. M. Rantamaki, P. C. de Vries, K. D. Zastrow, and the JET EFDA Contributors, Plasma Phys. Controlled Fusion **49**, 1931 (2007).

[41]J. Weiland and H. Nordman, in *Theory of Fusion Plasmas: Proceedings of the Joint Varenna-Lausanne International Workshop*, edited by A. Guthrie and R. K. Wakerling (Editrice Compositori for Societa Italiana di Fisica, Bologna, 1988).

[42]E. Asp, J. Weiland, X. Garbet, V. Parail, P. Strand, and the JET EFDA Contributors, Plasma Phys. Controlled Fusion **49**, 1221 (2007).

[43]J. Weiland, E. Asp, X. Garbet, P. Mantica, V. Parail, P. Thomas, W. Suttrop, T. Tala, and the EFDA-JET Contributors, Plasma Phys. Controlled Fusion **47**, 441 (2005).

[44]URL http://pecos.ph.utexas.edu/~vortex.

[45]T. Watanabe, H. Sugama, and W. Horton, Phys. Plasmas **14**, 022502 (2007).